An assessment of Southern Hemisphere extra-tropical cyclones in ERA5 using WindSat

Cameron McErlich[1], Adrian McDonald[1,2], James Renwick[3], and Alex Schuddeboom[1]

[1]School of Physical and Chemical Sciences, University of Canterbury, Christchurch, New Zealand
[2]Gateway Antarctica, University of Canterbury, Christchurch, New Zealand
[3]Victoria University of Wellington, School of Geography, Environment and Earth Science, Wellington, New Zealand

Key Points:

- Cyclone composites derived from ERA5 and WindSat show strong spatial correlations and small relative biases for winds and water vapour
- In the cold sector ERA5 underestimates cloud liquid water yet overestimates precipitation, while warm sector precipitation is underestimated
- Our comparison with WindSat shows that ERA5 represents the cyclone lifecycle well

Corresponding author: Cameron McErlich, cameron.mcerlich@pg.canterbury.ac.nz

Abstract

ERA5 reanalysis output is compared to WindSat measurements over cyclones at Southern Hemisphere mid- to high-latitudes. WindSat provides an independent measure of how well ERA5 represents cyclones, as WindSat is not assimilated into ERA5. We implement a tracking scheme to identify cyclone centres and tracks, before using cyclone composites to match concurrent data in ERA5 and WindSat. We find that both ERA5 and WindSat show comparable spatial structures for low level wind speed, total column water vapour, cloud liquid water and precipitation. Compared to WindSat, ERA5 underestimates total column water vapour by up to 5% and cloud liquid water by up to 40%. ERA5 underestimates precipitation in the warm sector by up to 15%, but overestimates in the cold sector by up to 60%. Similar biases in ERA5 are seen when comparing to AMSR-E data, even though AMSR-E radiances are assimilated into ERA5. Comparing ERA5 and WindSat across the cyclone lifecycle, a strong correlation is seen across the cyclone as it deepens and reaches peak intensity, before slightly declining as the cyclone decays. In the cold sector ERA5 shows underestimation of cloud liquid water, yet overestimates precipitation at all lifecycle stages. However, in the warm sector precipitation is underestimated. This potentially suggests the presence of biases within the ERA5 parameterisations of cloud and precipitation causing a disconnect between the two. Despite this, ERA5 shows strong correlation with WindSat and determines cyclone structure well across the cyclone lifecycle, showing its value for use in cyclone compositing analysis.

Plain Language Summary

Extra-tropical cyclones play a major role in the circulation within the atmosphere which acts to transfer heat towards the poles. Here we assess the representation of extra-tropical cyclone within the ERA5 reanalysis by comparing with observations made by the WindSat satellite. Because WindSat data is not used as input to the ERA5 model, it provides an independent measure of the quality of ERA5. By tracking low pressure cyclone centres, we can identify a set of cyclones which can then be used to determine the average behaviour of a cyclone. We find that both ERA5 and WindSat show similar features across the cyclone for near surface wind speed, water vapour, cloud liquid water and rainfall. However, ERA5 shows discrepancies with Windsat with underestimates of cloud liquid water and overestimates rainfall in the cold sector of the cyclone. Interestingly, rainfall is underestimated in the warm sector of cyclones in ERA5. When breaking the cyclones into lifecycle stages representing deepening, peak intensity and decay, ERA5 and WindSat once again show good agreement, although biases in cloud liquid water and rainfall persist. Overall ERA5 simulates cyclone structure well throughout their lifecycle.

1 Introduction

Extra-tropical cyclones (hereafter referred to as cyclones) are key components of the atmospheric general circulation due to their ability to transport large quantities of heat, moisture, and momentum. The baroclinc instability which feeds cyclones largely balances the planetary budgets of energy (Trenberth & Stepaniak, 2004) and moisture (Held & Soden, 2006) at mid-latitudes. The meteorology of the Southern Ocean is also dominated by the presence of these systems (Hoskins & Hodges, 2005) and their associated frontal systems (Berry et al., 2011; Utsumi et al., 2017). Cyclones are a conspicuous form of extra-tropical weather as their passage is associated with strong winds, precipitation, and temperature changes (Papritz et al., 2014). Additionally, cyclones strongly affect the mid-latitude distribution of water vapour, cloud and precipitation. Clouds associated with these systems also make up a significant portion of the total cloud field over the Southern Ocean (Haynes et al., 2011). Thus, these systems also have a major impact on the radiative balance in the region (Bodas-Salcedo et al., 2012).

Catto et al. (2012); Hawcroft et al. (2012); Utsumi et al. (2017) have shown that up to 90% of precipitation in the mid-latitude storm tracks is associated with cyclones and their associated fronts. Catto et al. (2012) also shows that more precipitation is associated with fronts in the Southern Hemisphere than the Northern Hemisphere. Pfahl and Wernli (2012) identified that a high percentage of precipitation extremes (up to 80%) are also found to be directly related to cyclones. Utsumi et al. (2017) also show large amounts of extreme precipitation in mid-latitude regions are associated with cyclones. When analysing cyclones over the US West Coast, (Zhang et al., 2019) found that 45% of cyclones have an associated atmospheric river which can enhance the precipitation and latent heat release and contributes to the deepening of the cyclone.

Satellite and ground-based observations are invaluable tools for the analysis of cyclone structure, and these different sources of data has led to development of several competing conceptual models (e.g., Carlson, 1980; Browning, 1997; Semple, 2003). Semple (2003) demonstrates how these conceptual models can be used at each phase in the cyclone lifecycle to provide a description of the physical processes occurring within the system and the range of evolution pathways. However, the lack of generality of case studies means they cannot easily be used to evaluate conceptual or numerical models (Jakob, 2003). Another assessment method uses a cyclone centered compositing methodology to create average information from a large number of cyclones. Aggregating atmospheric features over a large dataset allows a statistical measure of a model's ability to represent the large-scale dynamical processes and air flows, as well as their influence on moisture around these systems.

Many studies have used reanalysis datasets to study the structure and evolution of cyclones. Reanalyses assimilate observational data into a dynamical model framework, which can causes issues in the representation of atmospheric variables such as precipitation (Herold et al., 2016). However, they have good spatial and temporal coverage, which is especially useful over the Southern Ocean where observational datasets are sparse. Catto et al. (2010) identified that there are problems using reanalysis products for verification of model data, as precipitation in reanalysis datasets is strongly dependent upon the parameterisation in the underlying model. As a result, significant deficiencies are apparent when compared with observations, even in the most recent analyses. For example, Naud et al. (2020) investigated cyclonic precipitation in reanalyses and models compared to IMERGE satellite retrievals. They found ERA-Interim and MERRA-2 overestimate precipitation in the dry sector of the cyclones, and underestimate precipitation in the warm sector of the cyclone. Though they also note that the IMERG observational dataset might also exaggerate precipitation rates in vigorously ascending regions.

This study assesses the suitability of ERA5 in characterising extra-tropical cyclones in the Southern Hemisphere over mid to high latitudes (30S - 90S), while also displaying the utility of the WindSat dataset. Most of these cyclones are located over the Southern Ocean (See Figure 1). We compare output from the ERA5 reanalysis with WindSat data to identify the similarities and differences in the cyclone characteristics between these two products. WindSat is not assimilated into the ERA5 reanalyses and therefore provides an independent analysis of the quality of ERA5 over a wide range of geophysical variables. The focus on a single satellite instrument means that sampling differences associated with using multiple satellite instruments are also removed. Where possible we supplement this analysis with the AMSR-E dataset, but this does not provide an independent comparison with ERA5 as AMSR-E data has been assimilated into ERA5 (as highlighted in Hersbach et al., 2020). It does however allow us to examine the quality of the WindSat dataset.

We focus our attention over the Southern Ocean due to the many well established issues with the representation of cloud and precipitation in models over this region. Known issues of model representation over the Southern Ocean include too little cloud cover (e.g. Bodas-Salcedo et al., 2012; Schuddeboom et al., 2018; Kuma et al., 2020; McErlich et

al., 2021), excessive sunlight absorbed by the ocean surface (e.g. Trenberth & Fasullo, 2010; Hyder et al., 2018), a lack of clouds in the cold sectors of cyclones (e.g. Bodas-Salcedo et al., 2014), a lack of reflective supercooled water clouds (e.g. Bodas-Salcedo et al., 2016; Kuma et al., 2020), and an overestimation of the frequency and underestimation of the intensity in precipitation associated with fronts (Catto et al., 2015; Priestley et al., 2020). Beadling et al. (2020) also showed warm biased sea surface temperatures over the Southern Ocean still exist in CMIP6 models, which also effects the position of cyclones tracks (Priestley et al., 2020). Many of these model biases are not independent, such as shortwave radiative biases over the Southern Ocean forming from an underestimation of cloud within the models.

2 Datasets and Methods

2.1 ERA5

We use output from the ERA5 reanalysis (Hersbach et al., 2020), obtained from the Copernicus Climate Change Service (C3S, 2017). ERA5 is available on a 0.25° latitude/longitude grid and is utilized to examine cyclones over the Southern Hemisphere for the years 2003 - 2019 inclusive. This period is chosen to match with the available period for WindSat observations. Work detailed in McDonald and Cairns (2020) shows that ERA5 is consistent with a number of other reanalyses over the satellite era with little variation over that period, hence this period should be representative of reanalysis in general. ERA5 output is available on an hourly temporal resolution, but three hourly data was used in this study.

ERA-Interim has been used in a number of studies that focused on extra-tropical cyclones (e.g., Hodges et al., 2011; Naud et al., 2014, 2020), However, only a small number of cyclone related studies (Priestley et al., 2020, 2022) have used ERA5 thus far. Even fewer of these studies make use of the cyclone compositing methodology (Priestley & Catto, 2022). Significant work has already identified the utility of previous reanalyses, such as that in Hoskins and Hodges (2005) which used the 40-yr ECMWF reanalysis (ERA40) data to perform a detailed analysis of the Southern Hemisphere storm tracks. Given that ERA5 is a next-generation reanalysis with an even higher spatial resolution than these previous studies it is likely to be suitable for cyclone compositing.

2.2 WindSat

WindSat (Meissner & Wentz, 2009) is a multi-frequency polarimetric microwave radiometer developed by the Naval Research Laboratory for the National Polar-orbiting Operational Environmental Satellite System Integrated Program Office. WindSat was designed to demonstrate the capability of polarimetric microwave radiometry to measure the ocean surface wind vector from space and was launched on the Coriolis satellite on January 6th 2003 (Gaiser et al., 2004). This radiometer operates at five discrete frequencies (6.8, 10.7, 18.7, 23.8 and 37.0 GHz); all are fully polarimeteric except the 6.8 and 23.8 GHz channels that have only dual polarization. Despite a scheduled three year lifetime, WindSat continued to provide brightness temperature measurements of the ocean surface up until October 2020. The sampling of WindSat is densest towards high- and mid-latitudes which means that this instrument is well suited to examining cyclones over the Southern Ocean, and its long atmospheric record allows for a valuable comparison with ERA5.

Calibrated WindSat products are available from Remote Sensing Systems, and we use the v7.0.1 WindSat product in this study. Details about the retrievals used in these products are available in Gaiser et al. (2004) and Meissner and Wentz (2009). This retrieval uses measurements at C- and X-band frequencies coupled with a statistical algorithm to retrieve wind speeds that works in all weather conditions, a capability unique

to WindSat. In their work, they noted that since the model function and the retrieval algorithms are empirical, the satellite wind measurement accuracy has been quantified over a wide range of atmospheric conditions.

2.3 AMSR-E

In addition to the ERA5 and WindSat datasets, this study also uses data from the Advanced Microwave Scanning Radiometer for EOS (AMSR-E) onboard the polar-orbiting Aqua satellite. AMSR-E measures the microwave emission at six frequencies ranging from 6.9 to 89 GHz, with both vertical and horizontal polarization at all frequencies (Kawanishi et al., 2003). In particular, we use version 7 of the AMSR-E products available from Remote Sensing Systems. AMSR-E data is available between 2003 - 2011, or just over half of the observational period of WindSat. AMSR-E measurements of Brightness Temperature are assimilated into ERA5 (Hersbach et al., 2020), so it is not an independent dataset. However, AMSR-E still provides useful insight on the quality of WindSat data.

2.4 Cyclone tracking and compositing methodology

The cyclone tracking algorithm used in this study was detailed by Crawford and Serreze (2016) and has subsequently been used in a number of further studies (e.g., Koyama et al., 2017; Crawford & Serreze, 2017; Crawford et al., 2020; Hell et al., 2020). The algorithm uses sea level pressure information rather than 850 hPa vorticity. However, results are expected to be similar (Hoskins & Hodges, 2005; Neu et al., 2013; Simmonds & Rudeva, 2014), though it has been demonstrated that using the relative vorticity field potentially allows the identification of smaller scale cyclones earlier in their development (Hoskins & Hodges, 2005; Ulbrich et al., 2009). A detailed explanation of the cyclone tracking algorithm used can be found in Crawford and Serreze (2016), but the main steps are briefly detailed.

ERA5 mean sea level pressure (MSLP) information is first re-projected from the ERA5 latitude/longitude grid to a 50-km Equal-Area Scalable Earth Grid (EASE-Grid) in the Southern Hemisphere (Brodzik et al., 2012, 2014), centered over the South Pole. Cyclone centres were then identified between 2003 - 2019 with a temporal resolution of three hours. Existing research from Crawford et al. (2021) suggests that applying the cyclone tracking to MSLP data with a resolution shorter than 3 hours can lead to unrealistic splitting of the cyclone tracks, hence our decision to use ERA5 data at this resolution. The cyclone tracking algorithm determines local minima in the MSLP field and analyses the corresponding pressure gradient. A radii based threshold is used to identify whether it is a closed low pressure system and thus characterises a cyclone. A 150 $kmhr^{-1}$ propagation speed defines a maximum search radius for cyclone centres, and low pressure centers with corresponding centers in the previous time step being joined to identify continuous low pressure cyclone tracks. A maximum elevation of 500 m was used to make a mask such that cyclone centres identified above this height were ignored. Further criteria rejecting systems that have a lifespan shorter than 24 hours or a track length less than 100km are also applied. We also restrict cyclone tracks to those that spend some part of their lifetime at latitudes south of 30°S.

In order to assess the suitability of the cyclone tracking scheme over the Southern Hemisphere, and check ERA5's tracking capabilities, Figure 1a shows the track density over the defined domain. The track density is defined as the number of monthly cyclone tracks passing through a 500 km by 500 km area centered on each grid point. The highest density of cyclones is located around the Antarctic coastline. This pattern matches well with previous Southern Hemisphere cyclone track climatologies (Hoskins & Hodges, 2005; Bengtsson et al., 2006; Hodges et al., 2011).

Output from the cyclone tracking algorithms was used to transform a range of ERA5 data into a cyclone centered-coordinate system in the form of cyclone composites. The compositing process followed a similar methodology to that described in Catto et al. (2010). Firstly, the locations of the cyclone centre were identified using the tracking algorithm, to be used as the origin of the cyclone centred coordinate system. Data was extracted in a radius centered on each cyclone across the period of analysis. Due to the changing longitudinal extent of the cyclones as a function of latitude, the composite field was derived in polar coordinates, then interpolated onto a higher resolution polar coordinate grid to allow for smooth sampling across composites. Finally, individual composites are rotated so that the direction of propagation of the cyclone is chosen to be travelling eastward. Given the zonal westerly winds over the Southern Ocean many cyclones require little rotation. This step approximately aligns the position of the warm/cold fronts and the area of warm, moist air associated with them. While not all fronts will be at the same position relative to the direction of the cyclone, this rotation acts to focus the structure of the composite (Govekar et al., 2011).

Cyclone composites are derived over a circle of radius 2000 km. This radius is commonly used within previous work (e.g. Field & Wood, 2007; Field et al., 2008; Naud et al., 2012; Booth et al., 2018), although some studies use smaller radii (e.g. Catto et al., 2010; Flaounas et al., 2015; Naud et al., 2020; Sinclair et al., 2020). Some studies use a slightly larger but comparable 20 degree region surrounding the cyclone (e.g. Bengtsson et al., 2009; Priestley & Catto, 2022). To assess the suitability of the compositing radius, Figure 1b displays the cumulative frequency of maximum cyclone radius observed across all cyclone tracks. The mean value for the distribution is 1000 km, while the 99.9th percentile value for the distribution is approximately 2700 km. Therefore, setting the compositing radius at 2000 km means that greater than 95% of cyclones will be fully represented in the compositing scheme across all stages of their lifecycle.

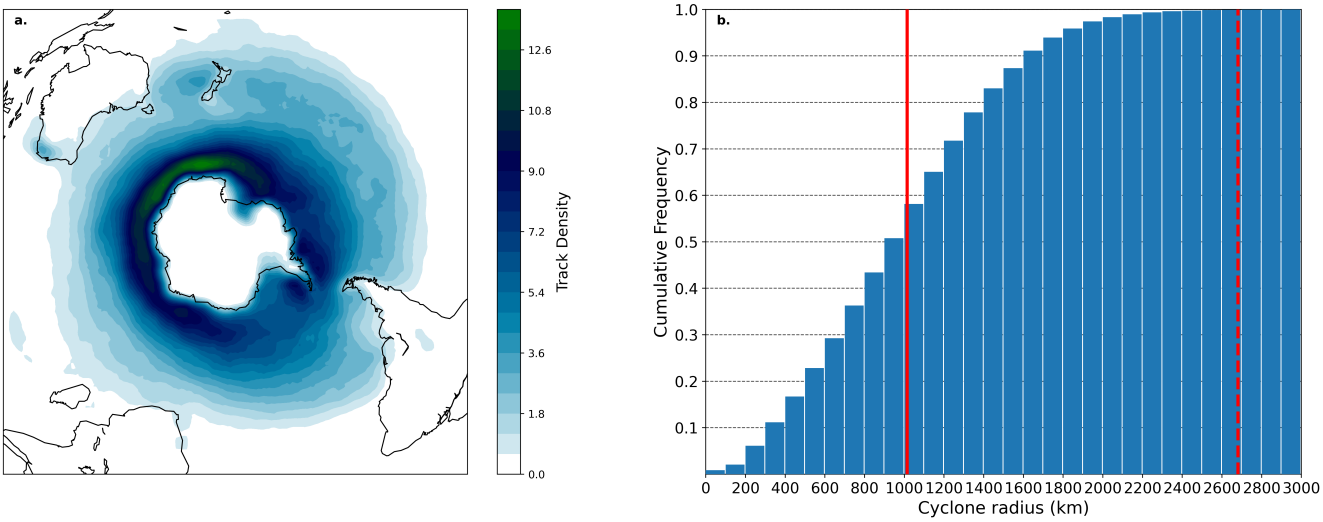

Figure 1. a) Cyclonic track density, defined as the monthly occurrence of tracks in 500km by 500 km box centred on each grid cell of the tracking domain. b) Cumulative frequency of occurrence of the maximum cyclone radii reached by each cyclone track. The solid (dashed) red line shows the mean (99.9th percentile) value of the distribution.

During the compositing process, WindSat data is only included based on two conditions. Firstly, observations are only included if they occur within one hour of the time defined by the ERA5 reanalysis. Secondly, only data that is also within a 2000 km ra-

dius of the cyclone centre are utilised. Reanalysis output were composited using the same method and are only included in the composite when corresponding WindSat data are available. Thus, we effectively use the presence of WindSat data to create a mask to reduce sampling biases. The same procedure is also completed to match the ERA5 and AMSR-E cyclone composites.

2.5 Analysis of cyclone lifecycle

In this study, cyclones are initially composited over all stages of development. The resulting composites cannot be expected to display characteristics of the well known development stages. To gain a greater understanding of the differences between ERA5 and WindSat fields, we partition the cyclones by their development phase relative to the time of maximum depth of the cyclone. Here depth is defined as the difference between the edge pressure and central pressure of the cyclone. In order to partition the cyclones into periods of deepening, peak intensity, and decay, a criterion based the deepening rate (DpDt, scaled by latitude) was also assessed. Cyclone tracks were only kept if the deepening rate changed from positive to negative around the point of peak intensity.

For each cyclone track that passed this criterion, three periods were defined. The period of peak intensity was defined as 6 hours either side of the time of maximum depth. The period of deepening was defined as measurements between 6 hours and 18 hours previous to the time of maximum depth. The period of decay was defined as measurements between 6 and 18 hours after the time of maximum depth. Tracks without measurements 18 hours before and after the point of peak intensity were rejected, causing a minimum cyclone lifespan of 36 hours to be considered. Different periods were investigated, but 12 hours was chosen to ensure a large proportion of tracks were not removed, while still filtering out cyclones without clear deepening and decay periods.

3 Results

3.1 Comparison of mean ERA5 and WindSat fields

Figure 2 displays cyclone-centred composites of 10m horizontal winds (UV10), Total Column Water Vapour (TCWV), Cloud Liquid Water (CLW) and Mean Total Precipitation Rate (MTPR) for both the ERA5 and WindSat data. Figure 2 also displays the difference between the two datasets, defined as ERA5 - WindSat. Cyclones have been tracked over the Southern Hemisphere, so the top of the composite corresponds to the equatorward sector. Similarly, the bottom corresponds to the poleward sector. Because of the rotation applied to the cyclone composites, the top of the composites may not align with north, so cardinal directions are not used to describe cyclone features.

Figure 2a shows that ERA5 UV10 winds display an axially asymmetric wind structure with the strongest winds above the cyclone centre in the upper left quadrant. The lowest winds are also close to the cyclone centre in the lower right quadrant. Field and Wood (2007) indicate that the clearly defined 'eye' at the centre of the cyclone in their analysis highlights the quality of the reanalysis derived cyclone locations and that the compositing methodology is working in their study. The clear 'eye' in our analysis therefore highlights the quality of the ERA5 derived cyclone positions and corresponding composites. Figure 2b shows WindSat 10m winds which also displays an axially asymmetric wind structure with similar features to those in the ERA5 reanalysis. Inspection of the differences in Figure 2c shows that ERA5 displays smaller 10m wind speeds compared to WindSat across nearly the entire composite, with the largest ERA5 underestimates occurring around the cyclone centre with underestimates up to 40% relative to WindSat. Looking at the wind vectors seen on Figure 2a-b, the direction of the wind vectors shows only slight changes across the composite between the ERA5 and WindSat datasets. When investigating the wind speed distributions of the zonal and meridional components

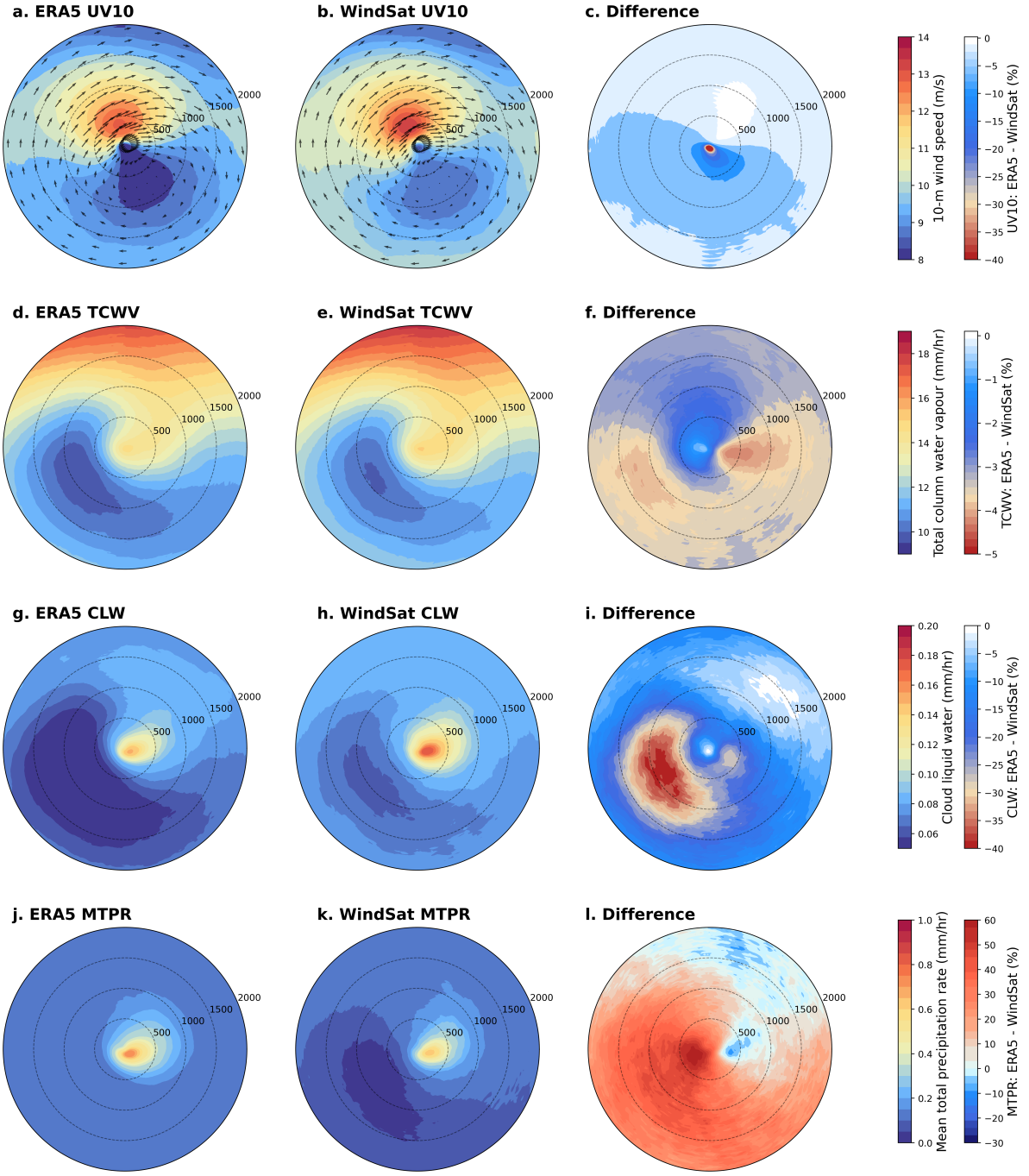

Figure 2. Cyclone-centred composites of 10 m horizontal winds derived from (a) ERA5 and (b) and WindSat composited from all cyclones observed between during 2003 to 2019 inclusive. (c) Shows the percentage difference between the two datasets (ERA5 - WindSat). (d - f) is the same as (a - c) but for total column water vapour. (g - i) is the same as (a - c) but for cloud liquid water. (j - i) is the same as (a - c) but for mean total precipitation rate. (a) and (b) also display wind vectors for ERA5 and WindSat respectively. Cyclone have been rotated so that the direction of storm propagation is towards the right.

separately (Supplementary Figure 1), WindSat displays a bimodal structure which is less pronounced in the ERA5 output. Assessing each quadrant individually shows the differences between ERA5 and WindSat are largest in the left quadrant of the cyclone.

The cyclone composite of ERA5 TCWV (Figure 2d) displays the expected contrast in TCWV between the dry poleward (bottom) and moist equatorward (top) portions of the cyclone. In particular, the pattern displays a tongue of dry air wrapped around the left flank of the cyclone which extends above the low pressure centre into the upper left quadrant. Correspondingly a warm moist tongue is observed to the right of the cyclone extending from the upper right quadrant toward the bottom of the cyclone. This distribution of TCWV is consistent with previous analyses, (Field & Wood, 2007; Naud et al., 2012, 2014) which display the contrast in humidity between the dry poleward and moist equatorward portions of the cyclone. For example, equivalent potential temperature composites shown in Catto et al. (2010) display a very similar pattern. Figure 2e shows WindSat TCWV composites are structurally similar to the patterns observed in ERA5, although Figure 2f shows that ERA5 has slightly lower TCWV across the entire composite (up to 5% relative difference). The largest differences occur in the poleward half of the composite, suggesting that the high water carrying capacity of the warm sector of the cyclone is very well captured well by ERA5. In particular, ERA5 shows lower values of TCWV in the dry tongue located in the lower left quadrant of the cyclone composite. The two datasets also show differences directly right of the cyclone centre, where the moist TCWV tongue in WindSat extends further poleward than in ERA5.

Figure 2g shows ERA5 CLW has a clear comma cloud structure, as identified in conceptual models (see Semple, 2003), with the tail of the comma in the upper right quadrant of the composite. Govekar et al. (2014) directly linked the three-dimensional distribution of clouds with the dynamics of a composite cyclone and quantified the relationships between them. In particular, they identified the distinct comma structures similarity to the vertical motion field derived from reanalysis. Supplementary Figure 2 shows that ERA5 vertical velocity matches with the shape of the comma cloud, agreeing with the previous work detailed in Govekar et al. (2014). Maximum cloud liquid water values are observed on the tip of the spiral structure in CLW in Figure 2g. These features are likely related to the warm conveyor belt (WCB), a stream of warm moist air that originates at low levels in the warm sector and travels parallel to the cold front (Harrold, 1973). When it reaches the surface warm front the WCB rises rapidly along moist isentropes. As this warm air ascends, it forms the frontal cloud and the cloud head. WindSat CLW (Figure 2h) displays the same comma-like structure as observed in the ERA5 output. Differences between the ERA5 and WindSat composite show lower CLW values in ERA5 across the entire composite (see Figure 2i). While a difference of up to 30% exists within the high CLW comma structure, the greatest underestimate in relative terms occurs in ERA5 (up to 40%) lies within the drier lower left quadrant where CLW values are lower.

ERA5 cyclone composites of MTPR in Figure 2j show that the spatial pattern of the rain rate is similar to the cloud liquid water pattern displayed in Figure 2g as might be expected. The rain rate therefore also displays a comma structure to the right of the cyclone centre with the tail of the comma extending into the upper right quadrant, a feature also been by WindSat (Figure 2k). A comparison between ERA5 and WindSat in Figure 2l shows the largest difference of up to 60% occur left of the cyclone center, where ERA5 has greater rain rates. This pattern may occur because the rain rate is greater in the poleward side of the composite, but also because the peak precipitation rate occurs further toward the left in ERA5 than in WindSat. This difference in the location of the comma cloud also produces a region in the upper right quadrant of the cyclone where WindSat has slightly greater rain rates than ERA5 with values up to 15% larger. Field and Wood (2007) have previously identified a broad correlation of the rain rate with the moist water vapour tongue, which they suggest represents the position of the the warm

conveyor belt, confirming that most of the rainfall is associated with this feature. We observe a similar relationship in the ERA5 output and WindSat observation. Notably, the difference seen between ERA5 and WindSat in the upper right quadrant of Figure 2l matches well with the position of the moist water vapour tongue seen in Figure 2d/e.

Thus far, we have not made any assumptions about whether the structures represented in ERA5 or WindSat are more representative of reality. In order to provide a further reference points we examine a second satellite dataset, AMSR-E. Figure 3 compares ERA5 output and AMSR-E data relative to the cyclone centre for TCWV, CLW and MTPR. Due to differences in the AMSR-E and WindSat/ERA5 windspeed products, the two were not compared. We use the WindSat WSPD_AW product derived using all channels and three separate algorithms to obtain winds in all weather conditions, which are not determined in AMSR-E.

Figure 3a-b shows that TCWV displays similar structure for ERA5 and AMSR-E. Figure 3c shows that ERA5 has consistently lower TCWV across the entire composite, with differences of up to 7%. This is a near identical pattern to the differences seen in Figure 2f where the biggest differences lie in the poleward half of the composite. These difference are seen despite AMSR-E data being assimilated into ERA5 (Hersbach et al., 2020). Figure 3d-f for CLW are also consistent with the patterns observed between ERA5 and WindSat (Figure 2i). For the MTPR, Figure 3i shows increased precipitation compared to ERA5 as seen on Figure 2l for WindSat. However, the upper right quadrant where ERA5 shows greater precipitation compared to AMSR-E is far weaker than that seen on Figure 2l for WindSat. Overall these results suggests the two satellite products are consistent with each other, which might be expected given that they are derived using similar retrieval schemes and work on similar principles. We therefore suggest that ERA5 displays small to medium size biases compared to observations, where it tends to underestimate the amount of moisture, yet overestimate precipitation in the drier sections of the cyclones.

3.2 Variability of fields

In addition to inspecting the mean values in the ERA5 output and the WindSat data for similarities and differences, examination of the zonal and meridional distribution of wind (Supplementary Figure 1) demonstrates that looking at other statistical properties can be useful. Standard deviation is determined separately for ERA5 and WindSat across each individual cyclone composite used to determine the averages displayed on Figure 2. Standard deviation is also determined separately for each individual grid point of the cyclone composite. Figure 4a displays a scatter plot of the standard deviation of ERA5 UV10 against those derived from WindSat measurements, for each point in the cyclone composite shown on Figure 2a-b. The two datasets compare well with each other, although ERA5 displays a slightly lower standard deviation in UV10 than WindSat.

Figure 4b shows the standard deviation of ERA5 TCWV against WindSat estimates. The range of variability in ERA5 and WindSat again matches very well with most values falling around the one-to-one line. A linear least squares fit shows that the gradient and intercept are 0.95 and 0.044, respectively. Thus, the variability in the standard deviation is very well captured with only a slight underestimate of the observed WindSat value by ERA5.

Figure 4c displays the relationship between the standard deviation of CLW derived from ERA5 and WindSat. The values from ERA5 and WindSat display far less correspondence than UV10 and TCWV, with the standard deviations in ERA5 being significantly lower that those in WindSat across the same regions of the composite. The region of worst agreement is close to the cyclone centre where CLW is highest. Figure 4d displays the relationship between the standard deviation of MTPR derived from ERA5

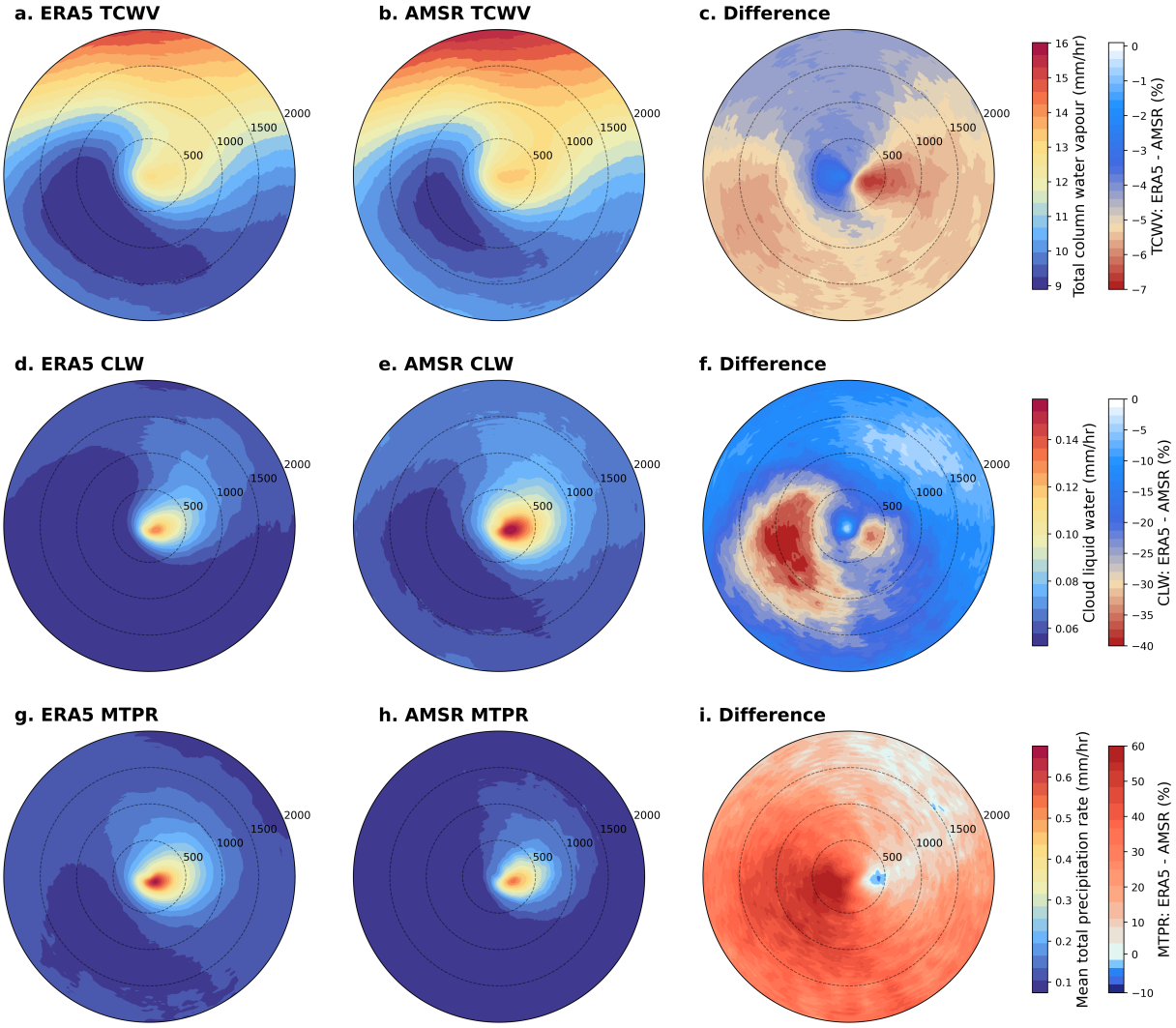

Figure 3. Cyclone-centred composites of TCWV from (a) ERA5 and (b) and AMSR-E composited from all cyclones observed between during 2003 to 2011 inclusive. (c) Shows the percentage difference between the two datasets (ERA5 - AMSR-E). (d - f) is the same as (a - c) but for CLW. (g - i) The same as (a - c) but for MTPR.

and WindSat. ERA5 shows lower variability than WindSat across almost all areas of the cyclone composites, displaying a slight improvement relative to the CLW, although close to the cyclone centre there is still significant variability.

For TCWV and UV10, both the mean (Figure 2c/f) and standard deviation (Figure 4a/b) of the TCWV and UV10 are very similar in ERA5 and WindSat. However, CLW and MTPR show much greater differences in the mean (Figure 2i/l) and standard deviation (Figure 4c/d). This means that the differences between CLW and MTPR between the ERA5 and the WindSat shown in Figure 2i/l are not likely to be directly driven by biases in TCWV, the advection of moisture, or the divergence and convergence of the horizontal winds.

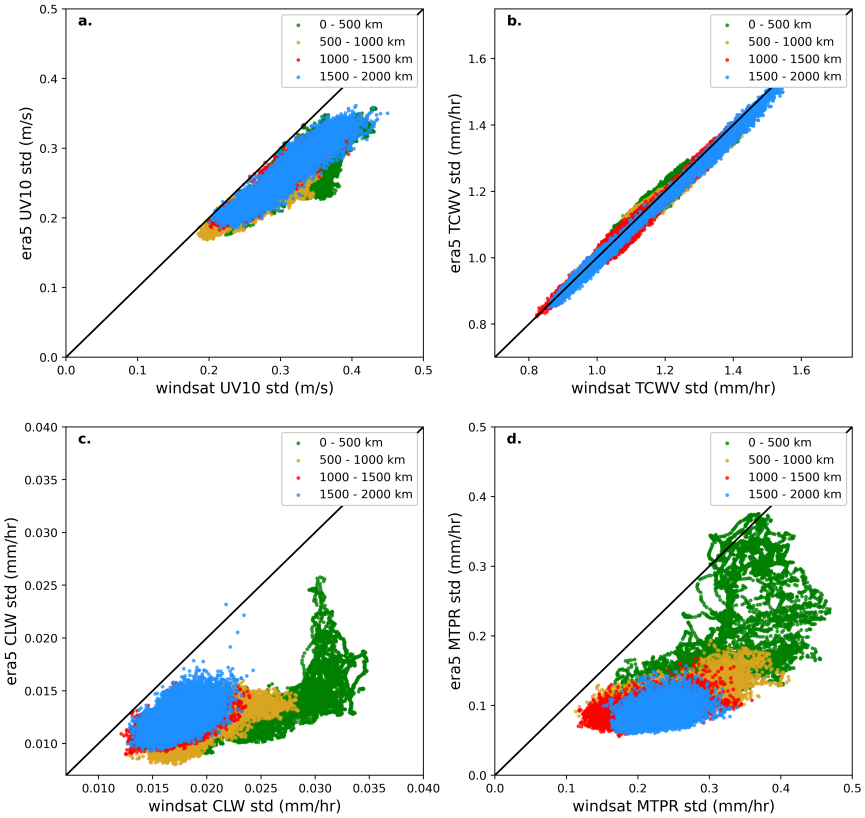

Figure 4. Scatter plot of the standard deviation compared at each point across the composite in ERA5 and WindSat for (a) UV10, (b) TCWV, (c) CLW and (d) MTPR. Points have been coloured based on the distance from the cyclone centre.

3.3 Representation of cyclone across lifecycle

Our composite analysis reveals distinct patterns in the distribution of water vapour, cloud, and precipitation near cyclones, which are reproduced in ERA5 and WindSat in Figure 2. However, distinct differences exist in these patterns as a function of lifecycle stage, strength, and deepening rate, as moisture convergence strongly depends on the cyclone's velocity field (e.g. Klein & Jakob, 1999; Field & Wood, 2007; Naud et al., 2012). We analyse cyclone composites for ERA5 and WindSat across regions of deepening, peak intensity and decay related to the depth of the cyclone. This provides a comparison of how structure changes in each datasets as the cyclone evolves, and how patterns differ between the two. This analysis is undertaken on a subset of the cyclone composites shown in Figure 2 which display clear periods of deepening, peak intensity and decay around the point of maximum cyclone depth.

Figure 5 displays the TCWV field from ERA5 (Figure 5a-c) and WindSat (Figure 5d-f) for the three different phases of the cyclone, while Figure 5g-i displays the percentage difference between the two. The amount of moisture in the warm sector decreases throughout the cyclone lifecyle in both ERA5 and WindSat. In particular, both show a weakening of the warm moist water vapour tongue, while the dry tongue strengthens and propagates further into the upper half of the composite. This behavior likely suggests frontal occlusion as the cyclone begins to weaken. Figure 5g-i shows that ERA5 always has lower TCWV than WindSat, with larger relative differences in the poleward area of the composite where ERA5 shows drier air. During the deepening phase, differ-

ences of up to 5% show comparable structure to that seen in Figure 2f with a bias in the position of the warm moist water vapour tongue. In order to compare how differences between ERA5 and WindSat change across cyclone lifecycle, Figure 5g-i also display the absolute mean bias averaged across the composite. As the cyclone reaches peak intensity and begins to decay, the absolute mean bias in ERA5 increases negligibly from 3.1% to 3.2%.

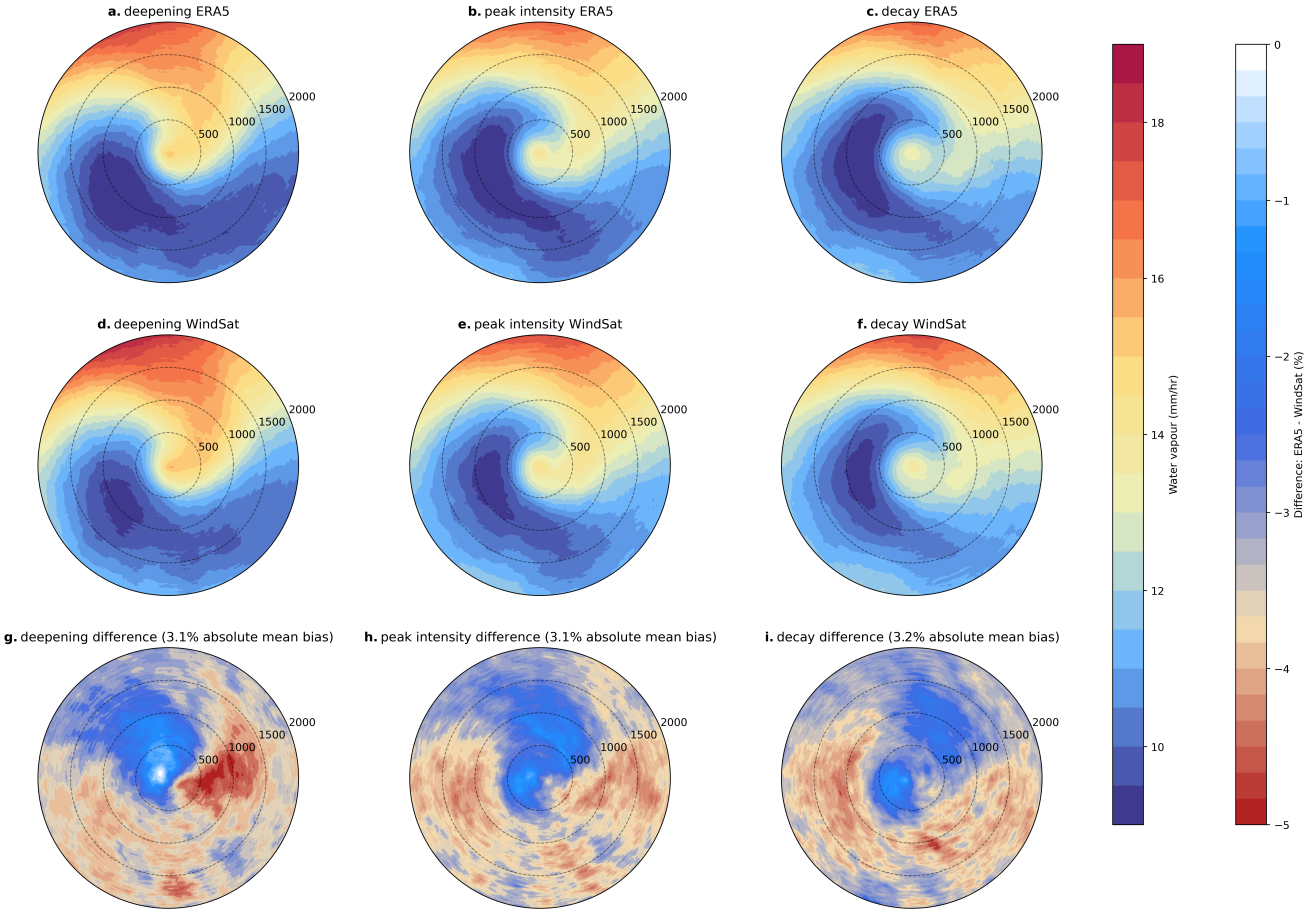

Figure 5. Cyclone composites of of TCWV partitioned into the deepening, peak intensity, and decay regions for a - c) ERA5, d - f) WindSat and g - i) the difference between the two.

Figure 6 shows cyclone composites for cloud liquid water derived similarly to Figure 5. CLW decreases over the cyclone lifecycle in both datasets, with a section of dry air strengthening and wrapping around the cyclone centre. Examination of patterns in ERA5 (Figure 6a-c) and WindSat (Figure 6d-f) shows general agreement with the patterns observed in Figure 5, where areas of high CLW match well with the moist water vapour tongue. Differences between ERA5 and WindSat in Figure 6g-i show that ERA5 almost always has lower CLW than WindSat across all stages of the lifecycle with differences of up to 60% associated with the driest region of the composite. The exception to this is the moist upper right quadrant of the cyclone where ERA5 shows CLW values up to 15% larger than WindSat. These relative differences are greater than the maximum underestimation (overestimation) in ERA5 CLW seen on Figure 2i of 40% (0%). Another notable feature is that as the comma cloud structure begins to rotate and dissipate, the pattern in the difference also rotates as the drier region moves into the equatorward portion of the composite. When looking at how the differences between ERA5

and WindSat change throughout the lifecycle, the absolute mean bias decreases slightly from 17.5% to 15.8%.

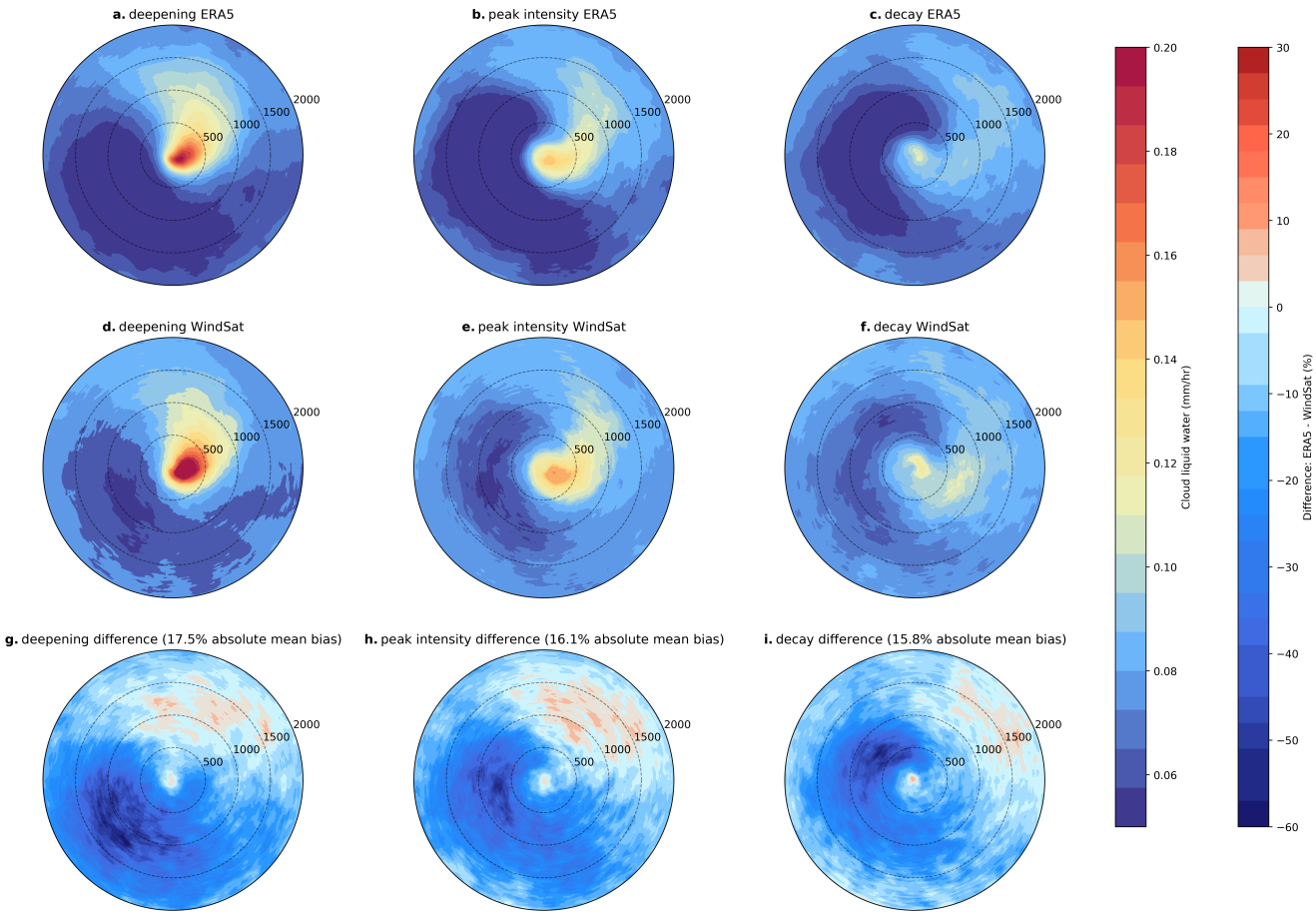

Figure 6. Cyclone composites of of CLW partitioned into the deepening, peak intensity, and decay regions regions for a - c) ERA5, d - f) WindSat and g - i) the difference between the two.

Figure 7 shows cyclone composites at different periods of the cyclone lifecyle for the mean total precipitation rate. Examination of the ERA5 and WindSat data in Figure 7a-c and 7d-e, respectively, shows the comma-cloud structure in MTPR weakens over the cyclone lifecycle in both datasets. A dry column pushes deeper into the cyclone from the poleward sector and the comma cloud rotates in a clockwise direction. Examination of the differences between ERA5 and WindSat in Figure 7g-i show ERA5 predominantly overestimates MTPR in the cold sector of the cyclone, while underestimating within the warm sector. The greatest differences of up to $\pm 70\,\%$ are observed during the deepening phase of the cyclone, but then begin to blur and reduce as the cyclone reaches peak intensity and enters the decay period. Again, behavior suggests frontal occlusion as the cyclone begins to weaken. Overestimation in MTPR is comparable to that in Figure 2l of 60%, but breaking analysis into periods of the cyclone lifecycle shows a greater underestimation of ERA5 MTPR compared to WindSat. This is most pronounced within the warm sector of the cyclone, where maximum underestimation of 30% on Figure 2l increases to 70% on Figure 7. However, the absolute mean bias only increases slightly from 28.4% to 29.6% throughout the cyclone lifecycle, where a decrease in the warm sector underestimation is offset by an increase in overestimation elsewhere within the cyclone composite.

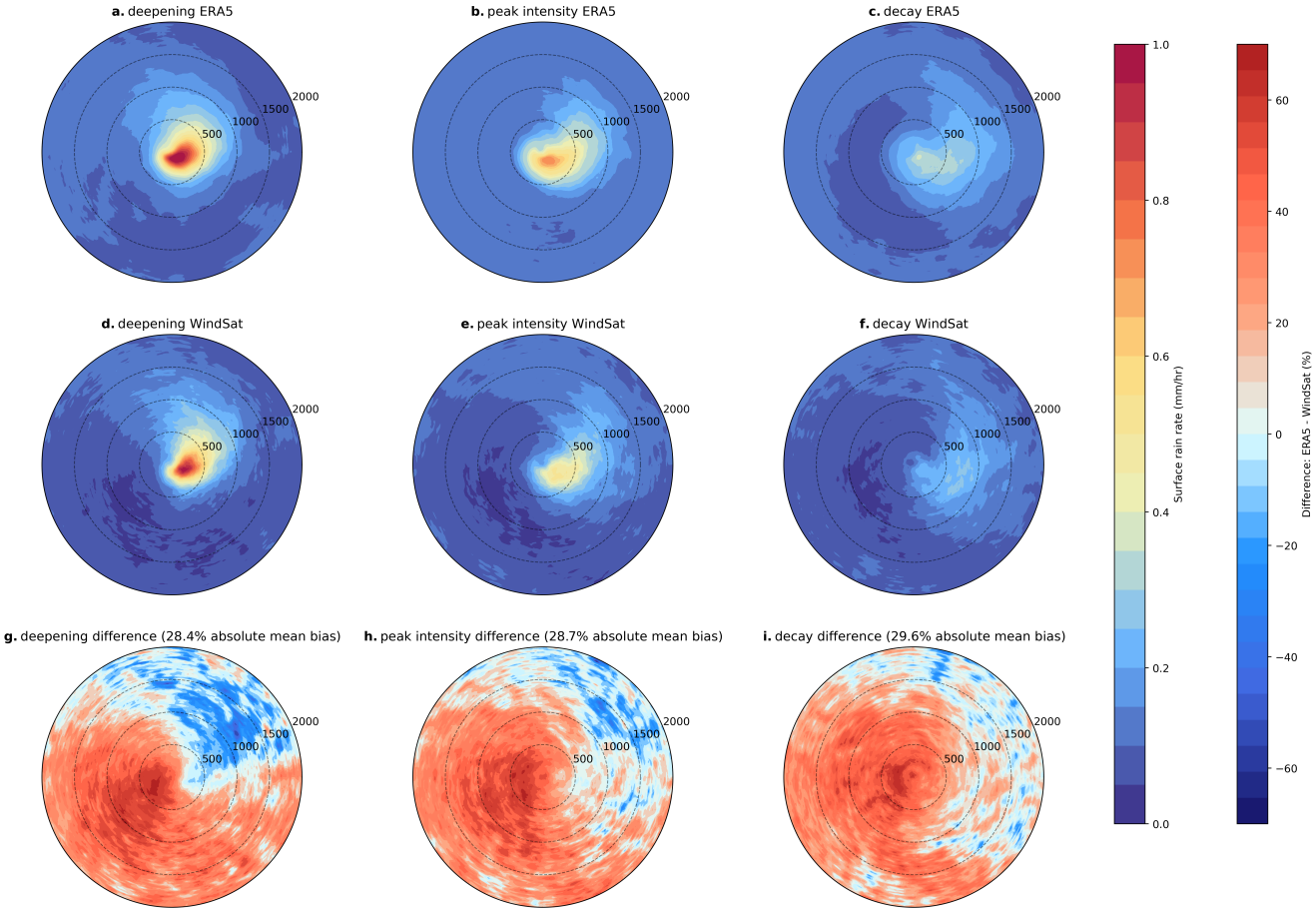

Figure 7. Cyclone composites of of MTPR partitioned into the deepening, peak intensity, and decay regions regions for a - c) ERA5, d - f) WindSat and g - i) the difference between the two.

Despite differences seen across Figures 5, 6 and 7, ERA5 and WindSat show similar spatial structure in each variable. In order to provide a more quantitative comparison, Figure 8 shows the Pearson correlation coefficient (r) between the ERA5 and WindSat spatial patterns, determined using a linear least-squares regression. Overall, ERA5 and WindSat display the best agreement within the deepening region with correlation coefficients above 0.9. Agreement reduces in CLW and MTPR as the cyclone evolves, with lower agreement in the peak intensity region and the lowest agreement within the decay region. Comparing the TCWV composites shows a correlation coefficient of almost 1 across all regions, which is unsurprising given the largest differences between the two are 5% and that there is assimilation of AMSR-E and other radiances which are sensitive to TCWV. CLW correlation is slightly poorer with weakest correlation during the decay period of 0.93. Although still strong, MTPR correlation is the lowest of the three variables examined with a correlation coefficient of 0.8 during the decay period. Correlation decreases moving from TWCV to CLW and MTPR, potentially indicating additive biases in the parameterisation of rainfall generating processes within ERA5.

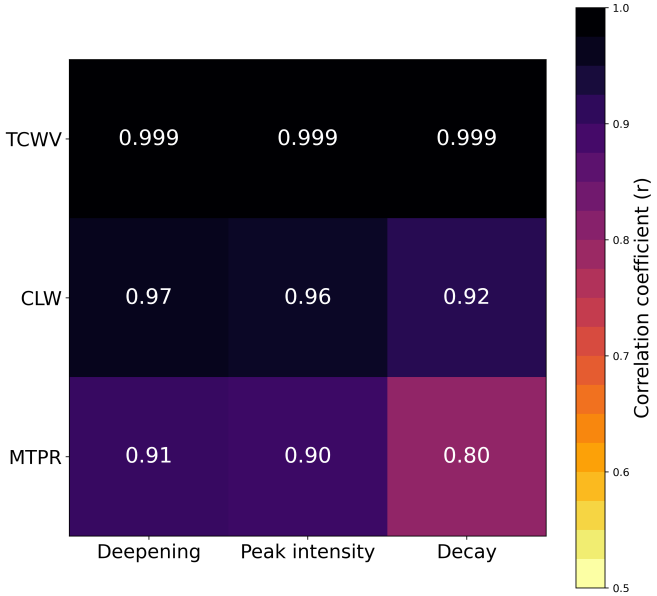

Figure 8. The correlation coefficient between ERA5 and WindSat for the TCWV, CLW and MPTR variables across cyclone lifecycle using a linear least-squares regression. Correlation is determined spatially across each grid point in the cyclone composites.

4 Discussion and Conclusion

ERA5 reanalysis output of 10m horizontal winds, total column water vapour, cloud liquid water, and mean total precipitation rate over the Southern Ocean are used to form cyclone composites to derive an integrated viewpoint of cyclone features. These composites are then compared with those derived from WindSat and AMSR-E radiometer measurements. Because WindSat is not assimilated into ERA5, it provides an independent measure of how well ERA5 represents cyclonic structure and cyclone evolution. AMSR-E radiances are assimilated into ERA5, but still provide a useful comparison.

A comparison between the mean horizontal wind speed cyclone composites calculated from ERA5 output and from WindSat data displays very similar structures (Figure 2a-b), but ERA5 shows slightly lower wind speeds in general compared to WindSat. More detailed inspection of the zonal and meridional components of the wind shows that the distributions between the ERA5 and WindSat data can be quite different, with ERA5 failing to fully reproduce the bimodal wind speed distribution displayed in WindSat (Supplementary Figure 1). This may provide evidence that small mesoscale features are not adequately simulated in the ERA5 reanalysis. Recent work, Priestley and Catto (2022), applied the cyclone compositing methodology to CMIP6 and HighResMIP models compared to baseline composites produced using ERA5. They found that HighResMIP models underestimated lower tropospheric winds compared to ERA5, although HighResMIP compared better. Given that ERA5 displays lower winds than WindSat, these models may have slightly larger issues with the representation of wind speed than identified in that work.

Examination of the TCWV and CLW fields demonstrate that ERA5 manages to replicate the structure of the corresponding WindSat cyclone composites well. However, we also show that both TCWV and CLW is lower in ERA5 over almost the entire region of the composite, although the TCWV differences (up to 5%) are far smaller than those in the CLW (up to 40%). Analysis on Figure 5 and Figure 6 shows that the TCWV

spatial structure in WindSat and ERA5 show good correspondence with those for CLW. This suggests that biases in the parameterisation of cloud are likely the driver of the large differences in CLW relative to the differences in TCWV, despite the assimilation of radiances from AMSR-E which likely constrain both TCWV and CLW. These cloud biases between ERA5 and WindSat would lead to variations between the two in the amount of water vapour condensing into liquid droplets. Further comparison between ERA5 and AMSR-E data on Figure 3 shows similar underestimates as identified with the WindSat data. A good match between the two satellite datasets highlights the utility of the WindSat dataset.

When comparing cyclone composites of the precipitation rate (Figure 2j-i), the biggest differences of up to 60% occur slightly to the left of the cyclone centre, where ERA5 is shown to have a greater maximum precipitation rate than WindSat. In part, these difference occur because the peak precipitation in ERA5 is seen to be shifted futher left compared to WindSat. However, these regions where ERA5 is overestimating MTPR compared to WindSat correspond to regions where it underestimates both CLW and TCWV. These differences are also seen when comparing ERA5 with the AMSR-E dataset. Our results agree with Naud et al. (2020), who found ERA-Interim and MERRA-2 overestimate precipitation in the dry sector of the cyclones, and underestimate precipitation in the warm sector of the cyclone. These biases appear to remain within the ERA5 reanalysis product, and points to possible continuing parameterisation issues within ERA5, given the agreement between WindSat and the AMSR-E product.

When breaking TCWV, CLW and MTPR into stages of the cyclone lifecycle (Figures 5, 6, 7), these biases remain, and strengthen in the case of CLW and MTPR across the cyclone lifecycle. Although, for MTPR, a decrease in the underestimation of precipitation in the warm sector is offset by an increase in the overestimation of precipitation elsewhere within the cyclone composite. The dry poleward region of the cyclone shows the area of largest relative difference across all variables. The average bias increases slightly over cyclone lifecycle for the TCWV and MTPR and decreases slightly for CLW. Our results show that strongest rain rates occur in the deepening region before the cyclone reaches its maximum strength. This provides observational support for the idea that the release of latent heating associated with precipitation is an important contributor to the intensification of cyclones (Wernli et al., 2002; Ludwig et al., 2014; Binder et al., 2016). Booth et al. (2018) also found that maximum precipitation occurs before the cyclone reaches peak intensity 70% of the time, as well as a weakening in the comma like structure of precipitation through the cyclone lifecycles. This matches the structure seen on Figure 7, and suggests that ERA5 is adept at capturing the underlying changes in precipitation during the evolution of the cyclone.

In summary this study shows that ERA5 represents the near surface wind speeds and total column water vapour of extra-tropical cyclones well. Representation of cloud liquid water and precipitation rate is poorer; ERA5 underestimates cloud liquid water, yet overestimates precipitation in the cold sectors of the cyclone. Warm sector precipitation is also underestimated in ERA5 compared to WindSat. Despite biases seen in ERA5 compared to WindSat, both datasets show similar spatial structure across the cyclone lifecycle for TCWV, CLW and MTPR. Quantifying this using a Pearson correlation shows strong agreement between the two datasets, although agreement lessens during the decay period of the cyclone for CLW and MTPR. This suggests that ERA5 is adequately determining cyclone structure across a range of cyclonic life stages and is valuable for use in cyclone compositing analysis.

Acknowledgments

The ERA5 reanalysis products were obtained from the Copernicus Climate Data Store (https://cds.climate.copernicus.eu/). WindSat v7.0.1 was obtained from Remote Sensing Systems (https://www.remss.com/missions/windsat/). Data used to visualise the

figures is available at https://doi.org/10.5281/zenodo.7539490. We would also like to acknowledge funding from the Ministry of Business, Innovation and Employment (MBIE), New Zealand, through the Whakahura project.

References

Beadling, R. L., Russell, J. L., Stouffer, R. J., Mazloff, M., Talley, L. D., Goodman, P. J., ... Pandde, A. (2020). Representation of southern ocean properties across coupled model intercomparison project generations: Cmip3 to cmip6. *Journal of Climate*, *33*(15), 6555 - 6581. Retrieved from `https://journals.ametsoc.org/view/journals/clim/33/15/jcliD190970.xml` doi: 10.1175/JCLI-D-19-0970.1

Bengtsson, L., Hodges, K. I., & Keenlyside, N. (2009). Will extratropical storms intensify in a warmer climate? *Journal of Climate*, *22*(9), 2276 - 2301. Retrieved from `https://journals.ametsoc.org/view/journals/clim/22/9/2008jcli2678.1.xml` doi: 10.1175/2008JCLI2678.1

Bengtsson, L., Hodges, K. I., & Roeckner, E. (2006). Storm tracks and climate change. *Journal of Climate*, *19*(15), 3518 - 3543. Retrieved from `https://journals.ametsoc.org/view/journals/clim/19/15/jcli3815.1.xml` doi: 10.1175/JCLI3815.1

Berry, G., Reeder, M. J., & Jakob, C. (2011). A global climatology of atmospheric fronts. *Geophysical Research Letters*, *38*(4). doi: https://doi.org/10.1029/2010GL046451

Binder, H., Boettcher, M., Joos, H., & Wernli, H. (2016). The role of warm conveyor belts for the intensification of extratropical cyclones in northern hemisphere winter. *Journal of the Atmospheric Sciences*, *73*(10), 3997 - 4020. doi: 10.1175/JAS-D-15-0302.1

Bodas-Salcedo, A., Hill, P., Furtato, K., Williams, K., Field, P., Manners, J., & Hyder, P. (2016). Large contribution of supercooled liquid clouds to the solar radiation budget of the southern ocean. *Journal of Climate*, *29*(11), 4213-4228. doi: 10.1175/jcli-d-15-0564.1

Bodas-Salcedo, A., Williams, K., Field, P., & Lock, A. (2012). The surface downwelling solar radiation surplus over the southern ocean in the met office model: The role of midlatitude cyclone clouds. *Journal of Climate*, *25*, 7467–7486. doi: 10.1175/jcli-d-11-00702.1

Bodas-Salcedo, A., Williams, K. D., Ringer, M. A., Beau, I., Cole, J. N. S., Dufresne, J. L., ... Yokohata, T. (2014). Origins of the solar radiation biases over the southern ocean in cfmip2 models. *Journal of Climate*, *27*, 41-56. doi: 10.1175/JCLI-D-13-00169.1

Booth, J. F., Naud, C. M., & Jeyaratnam, J. (2018). Extratropical cyclone precipitation life cycles: A satellite-based analysis. *Geophysical Research Letters*, *45*(16), 8647-8654. Retrieved from `https://agupubs.onlinelibrary.wiley.com/doi/abs/10.1029/2018GL078977` doi: https://doi.org/10.1029/2018GL078977

Brodzik, M. J., Billingsley, B., Haran, T., Raup, B., & Savoie, M. H. (2012). Ease-grid 2.0: Incremental but significant improvements for earth-gridded data sets. *ISPRS International Journal of Geo-Information*, *1*(1), 32–45. doi: 10.3390/ijgi1010032

Brodzik, M. J., Billingsley, B., Haran, T., Raup, B., & Savoie, M. H. (2014). Correction: Brodzik, m.j., et al. ease-grid 2.0: Incremental but significant improvements for earth-gridded data sets. isprs international journal of geo-information 2012, 1, 32–45. *ISPRS International Journal of Geo-Information*, *3*(3), 1154–1156. doi: 10.3390/ijgi3031154

Browning, K. A. (1997). The dry intrusion perspective of extra-tropical cyclone development. *Meteorological Applications*, *4*(4), 317–324. doi:

10.1017/S1350482797000613

Carlson, T. N. (1980). Airflow through midlatitude cyclones and the comma cloud pattern. *Monthly Weather Review*, *108*(10), 1498 - 1509. doi: 10.1175/1520-0493(1980)108⟨1498:ATMCAT⟩2.0.CO;2

Catto, J. L., Jakob, C., Berry, G., & Nicholls, N. (2012). Relating global precipitation to atmospheric fronts. *Geophysical Research Letters*, *39*(10). doi: https://doi.org/10.1029/2012GL051736

Catto, J. L., Jakob, C., & Nicholls, N. (2015). Can the cmip5 models represent winter frontal precipitation? *Geophysical Research Letters*, *42*(20), 8596-8604. doi: https://doi.org/10.1002/2015GL066015

Catto, J. L., Shaffrey, L. C., & Hodges, K. I. (2010). Can climate models capture the structure of extratropical cyclones? *Journal of Climate*, *23*(7), 1621 - 1635. doi: 10.1175/2009JCLI3318.1

Crawford, A. D., Alley, K. E., Cooke, A. M., & Serreze, M. C. (2020). Synoptic climatology of rain-on-snow events in alaska. *Monthly Weather Review*, *148*(3), 1275 - 1295. doi: 10.1175/MWR-D-19-0311.1

Crawford, A. D., Schreiber, E. A. P., Sommer, N., Serreze, M. C., Stroeve, J. C., & Barber, D. G. (2021). Sensitivity of northern hemisphere cyclone detection and tracking results to fine spatial and temporal resolution using era5. *Monthly Weather Review*, *149*(8), 2581 - 2598. doi: 10.1175/MWR-D-20-0417.1

Crawford, A. D., & Serreze, M. C. (2016). Does the summer arctic frontal zone influence arctic ocean cyclone activity? *Journal of Climate*, *29*(13), 4977 - 4993. doi: 10.1175/JCLI-D-15-0755.1

Crawford, A. D., & Serreze, M. C. (2017). Projected changes in the arctic frontal zone and summer arctic cyclone activity in the cesm large ensemble. *Journal of Climate*, *30*(24), 9847 - 9869. doi: 10.1175/JCLI-D-17-0296.1

Field, P. R., Gettelman, A., Neale, R. B., Wood, R., Rasch, P. J., & Morrison, H. (2008). Midlatitude cyclone compositing to constrain climate model behavior using satellite observations. *Journal of Climate*, *21*(22), 5887 - 5903. doi: 10.1175/2008JCLI2235.1

Field, P. R., & Wood, R. (2007). Precipitation and cloud structure in midlatitude cyclones. *Journal of Climate*, *20*(2), 233 - 254. doi: 10.1175/JCLI3998.1

Flaounas, E., Raveh-Rubin, S., Wernli, H., Drobinski, P., & Bastin, S. (2015, May 01). The dynamical structure of intense mediterranean cyclones. *Climate Dynamics*, *44*(9), 2411-2427. doi: 10.1007/s00382-014-2330-2

Gaiser, P., St Germain, K., Twarog, E., Poe, G., Purdy, W., Richardson, D., ... Chang, P. (2004). The windsat spaceborne polarimetric microwave radiometer: sensor description and early orbit performance. *IEEE Transactions on Geoscience and Remote Sensing*, *42*(11), 2347-2361. doi: 10.1109/TGRS.2004.836867

Govekar, P. D., Jakob, C., & Catto, J. (2014). The relationship between clouds and dynamics in southern hemisphere extratropical cyclones in the real world and a climate model. *Journal of Geophysical Research: Atmospheres*, *119*(11), 6609-6628. doi: https://doi.org/10.1002/2013JD020699

Govekar, P. D., Jakob, C., Reeder, M. J., & Haynes, J. (2011). The three-dimensional distribution of clouds around southern hemisphere extratropical cyclones. *Geophysical Research Letters*, *38*(21). doi: https://doi.org/10.1029/2011GL049091

Harrold, T. (1973). Mechanisms influencing the distribution of precipitation within baroclinic disturbances. *Quart. J. Roy. Meteor. Soc.*, *99*, 232–251.

Hawcroft, M., Shaffrey, L., Hodges, K., & Dacre, H. (2012, 12). How much northern hemisphere precipitation is associated with extratropical cyclones? *Geophysical Research Letters*, *39*, 24809-. doi: 10.1029/2012GL053866

Haynes, J. M., Jakob, C., Rossow, W. B., Tselioudis, G., & Brown, J. (2011). Major characteristics of southern ocean cloud regimes and their effects

on the energy budget. *Journal of Climate*, *24*(19), 5061 - 5080. doi: 10.1175/2011JCLI4052.1

Held, I. M., & Soden, B. J. (2006). Robust responses of the hydrological cycle to global warming. *Journal of Climate*, *19*(21), 5686 - 5699. doi: 10.1175/JCLI3990.1

Hell, M. C., Gille, S. T., Cornuelle, B. D., Miller, A. J., Bromirski, P. D., & Crawford, A. D. (2020). Estimating southern ocean storm positions with seismic observations. *Journal of Geophysical Research: Oceans*, *125*(4), e2019JC015898. doi: https://doi.org/10.1029/2019JC015898

Herold, N., Alexander, L. V., Donat, M. G., Contractor, S., & Becker, A. (2016). How much does it rain over land? *Geophysical Research Letters*, *43*(1), 341-348. Retrieved from `https://agupubs.onlinelibrary.wiley.com/doi/abs/10.1002/2015GL066615` doi: https://doi.org/10.1002/2015GL066615

Hersbach, H., Bell, B., Berrisford, P., Hirahara, S., Horányi, A., Muñoz-Sabater, J., ... Thépaut, J.-N. (2020). The era5 global reanalysis. *Quarterly Journal of the Royal Meteorological Society*, *146*(730), 1999-2049. doi: https://doi.org/10.1002/qj.3803

Hodges, K. I., Lee, R. W., & Bengtsson, L. (2011). A comparison of extratropical cyclones in recent reanalyses era-interim, nasa merra, ncep cfsr, and jra-25. *Journal of Climate*, *24*(18), 4888 - 4906. Retrieved from `https://journals.ametsoc.org/view/journals/clim/24/18/2011jcli4097.1.xml` doi: 10.1175/2011JCLI4097.1

Hoskins, B. J., & Hodges, K. I. (2005). A new perspective on southern hemisphere storm tracks. *Journal of Climate*, *18*(20), 4108 - 4129. doi: 10.1175/JCLI3570.1

Hyder, P., Edwards, J. M., Allan, R. P., Hewitt, H. T., Bracegirdle, T. J., Gregory, J. M., ... Belcher, S. E. (2018, Sep 11). Critical southern ocean climate model biases traced to atmospheric model cloud errors. *Nature Communications*, *9*(1), 3625. Retrieved from `https://doi.org/10.1038/s41467-018-05634-2` doi: 10.1038/s41467-018-05634-2

Jakob, C. (2003). An improved strategy for the evaluation of cloud parameterizations in gcms [Journal Article]. *Bulletin of the American Meteorological Society*, *84*(10), 1387-+. doi: 10.1175/bams-84-10-1387

Kawanishi, T., Sezai, T., Ito, Y., Imaoka, K., Takeshima, T., Ishido, Y., ... Spencer, R. (2003). The advanced microwave scanning radiometer for the earth observing system (amsr-e), nasda's contribution to the eos for global energy and water cycle studies. *IEEE Transactions on Geoscience and Remote Sensing*, *41*(2), 184-194. doi: 10.1109/TGRS.2002.808331

Klein, S. A., & Jakob, C. (1999). Validation and sensitivities of frontal clouds simulated by the ecmwf model. *Monthly Weather Review*, *127*(10), 2514 - 2531. doi: 10.1175/1520-0493(1999)127⟨2514:VASOFC⟩2.0.CO;2

Koyama, T., Stroeve, J., Cassano, J., & Crawford, A. (2017). Sea ice loss and arctic cyclone activity from 1979 to 2014. *Journal of Climate*, *30*(12), 4735 - 4754. doi: 10.1175/JCLI-D-16-0542.1

Kuma, P., McDonald, A., Morgenstern, O., Alexander, S., Cassano, J., Garrett, A., ... Williams, J. (2020). Evaluation of southern ocean cloud in the hadgem3 general circulation model and merra-2 reanalysis using ship-based observations. *Atmospheric Chemistry and Physics Discussions*, *20*(11), 6607-6630. doi: 10.5194/acp-2019-201

Ludwig, P., Pinto, J. G., Reyers, M., & Gray, S. L. (2014). The role of anomalous sst and surface fluxes over the southeastern north atlantic in the explosive development of windstorm xynthia. *Quarterly Journal of the Royal Meteorological Society*, *140*(682), 1729-1741. doi: https://doi.org/10.1002/qj.2253

McDonald, A. J., & Cairns, L. H. (2020). A new method to evaluate reanalyses using synoptic patterns: An example application in the ross sea/ross ice

shelf region. *Earth and Space Science*, *7*(1), e2019EA000794. Retrieved from https://agupubs.onlinelibrary.wiley.com/doi/abs/10.1029/2019EA000794 doi: https://doi.org/10.1029/2019EA000794

McErlich, C., McDonald, A., Schuddeboom, A., & Silber, I. (2021). Comparing satellite- and ground-based observations of cloud occurrence over high southern latitudes. *Journal of Geophysical Research: Atmospheres*, *126*(6), e2020JD033607. Retrieved from https://agupubs.onlinelibrary.wiley.com/doi/abs/10.1029/2020JD033607 (e2020JD033607 2020JD033607) doi: https://doi.org/10.1029/2020JD033607

Meissner, T., & Wentz, F. J. (2009). Wind-vector retrievals under rain with passive satellite microwave radiometers. *IEEE Transactions on Geoscience and Remote Sensing*, *47*(9), 3065-3083. doi: 10.1109/TGRS.2009.2027012

Naud, C. M., Booth, J. F., & Genio, A. D. D. (2014). Evaluation of era-interim and merra cloudiness in the southern ocean. *Journal of Climate*, *27*(5), 2109 - 2124. doi: 10.1175/JCLI-D-13-00432.1

Naud, C. M., Jeyaratnam, J., Booth, J. F., Zhao, M., & Gettelman, A. (2020). Evaluation of modeled precipitation in oceanic extratropical cyclones using imerg. *Journal of Climate*, *33*(1), 95 - 113. Retrieved from https://journals.ametsoc.org/view/journals/clim/33/1/jcli-d-19-0369.1.xml doi: 10.1175/JCLI-D-19-0369.1

Naud, C. M., Posselt, D. J., & van den Heever, S. C. (2012). Observational analysis of cloud and precipitation in midlatitude cyclones: Northern versus southern hemisphere warm fronts. *Journal of Climate*, *25*(14), 5135 - 5151. doi: 10.1175/JCLI-D-11-00569.1

Neu, U., Akperov, M. G., Bellenbaum, N., Benestad, R., Blender, R., Caballero, R., ... Wernli, H. (2013). Imilast: A community effort to intercompare extratropical cyclone detection and tracking algorithms:. *Bulletin of the American Meteorological Society*, *94*(4), 529 - 547. doi: 10.1175/BAMS-D-11-00154.1

Papritz, L., Pfahl, S., Rudeva, I., Simmonds, I., Sodemann, H., & Wernli, H. (2014). The role of extratropical cyclones and fronts for southern ocean freshwater fluxes. *Journal of Climate*, *27*(16), 6205 - 6224. doi: 10.1175/JCLI-D-13-00409.1

Pfahl, S., & Wernli, H. (2012). Quantifying the relevance of cyclones for precipitation extremes. *Journal of Climate*, *25*(19), 6770 - 6780. doi: 10.1175/JCLI-D-11-00705.1

Priestley, M. D. K., Ackerley, D., Catto, J. L., & Hodges, K. I. (2022). Drivers of biases in the cmip6 extratropical storm tracks. part 1: Northern hemisphere. *Journal of Climate*, 1 - 37. doi: 10.1175/JCLI-D-20-0976.1

Priestley, M. D. K., Ackerley, D., Catto, J. L., Hodges, K. I., McDonald, R. E., & Lee, R. W. (2020). An overview of the extratropical storm tracks in cmip6 historical simulations. *Journal of Climate*, *33*(15), 6315 - 6343. doi: 10.1175/JCLI-D-19-0928.1

Priestley, M. D. K., & Catto, J. L. (2022). Improved representation of extratropical cyclone structure in highresmip models. *Geophysical Research Letters*, *49*(5), e2021GL096708. (e2021GL096708 2021GL096708) doi: https://doi.org/10.1029/2021GL096708

Schuddeboom, A., McDonald, A. J., Morgenstern, O., Harvey, M., & Parsons, S. (2018). Regional regime-based evaluation of present-day general circulation model cloud simulations using self-organizing maps. *Journal of Geophysical Research: Atmospheres*, *123*(8), 4259-4272. doi: 10.1002/2017jd028196

Semple, A. (2003). A review and unification of conceptual models of cyclogenesis. *Meteorological Applications*, *10*, 39-59.

Simmonds, I., & Rudeva, I. (2014). A comparison of tracking methods for extreme cyclones in the arctic basin. *Tellus A: Dynamic Meteorology and Oceanography*, *66*(1), 25252. doi: 10.3402/tellusa.v66.25252

Sinclair, V. A., Rantanen, M., Haapanala, P., Räisänen, J., & Järvinen, H. (2020). The characteristics and structure of extra-tropical cyclones in a warmer climate. *Weather and Climate Dynamics*, *1*(1), 1–25. Retrieved from `https://wcd.copernicus.org/articles/1/1/2020/` doi: 10.5194/wcd-1-1-2020

Trenberth, K. E., & Fasullo, J. T. (2010). Simulation of present-day and twenty-first-century energy budgets of the southern oceans. *Journal of Climate*, *23*(2), 440 - 454. doi: 10.1175/2009JCLI3152.1

Trenberth, K. E., & Stepaniak, D. P. (2004). The flow of energy through the earth's climate system. *Quarterly Journal of the Royal Meteorological Society*, *130*(603), 2677-2701. doi: https://doi.org/10.1256/qj.04.83

Ulbrich, U., Leckebusch, G. C., & Pinto, J. G. (2009, Apr 01). Extra-tropical cyclones in the present and future climate: a review. *Theoretical and Applied Climatology*, *96*(1), 117-131. doi: 10.1007/s00704-008-0083-8

Utsumi, N., Kim, H., Kanae, S., & Oki, T. (2017). Relative contributions of weather systems to mean and extreme global precipitation. *Journal of Geophysical Research: Atmospheres*, *122*(1), 152-167. doi: https://doi.org/10.1002/2016JD025222

Wernli, H., Dirren, S., Liniger, M. A., & Zillig, M. (2002). Dynamical aspects of the life cycle of the winter storm 'lothar' (24–26 december 1999). *Quarterly Journal of the Royal Meteorological Society*, *128*(580), 405-429. doi: https://doi.org/10.1256/003590002321042036

Zhang, Z., Ralph, F. M., & Zheng, M. (2019). The relationship between extratropical cyclone strength and atmospheric river intensity and position. *Geophysical Research Letters*, *46*(3), 1814-1823. doi: https://doi.org/10.1029/2018GL079071

Figure 1.

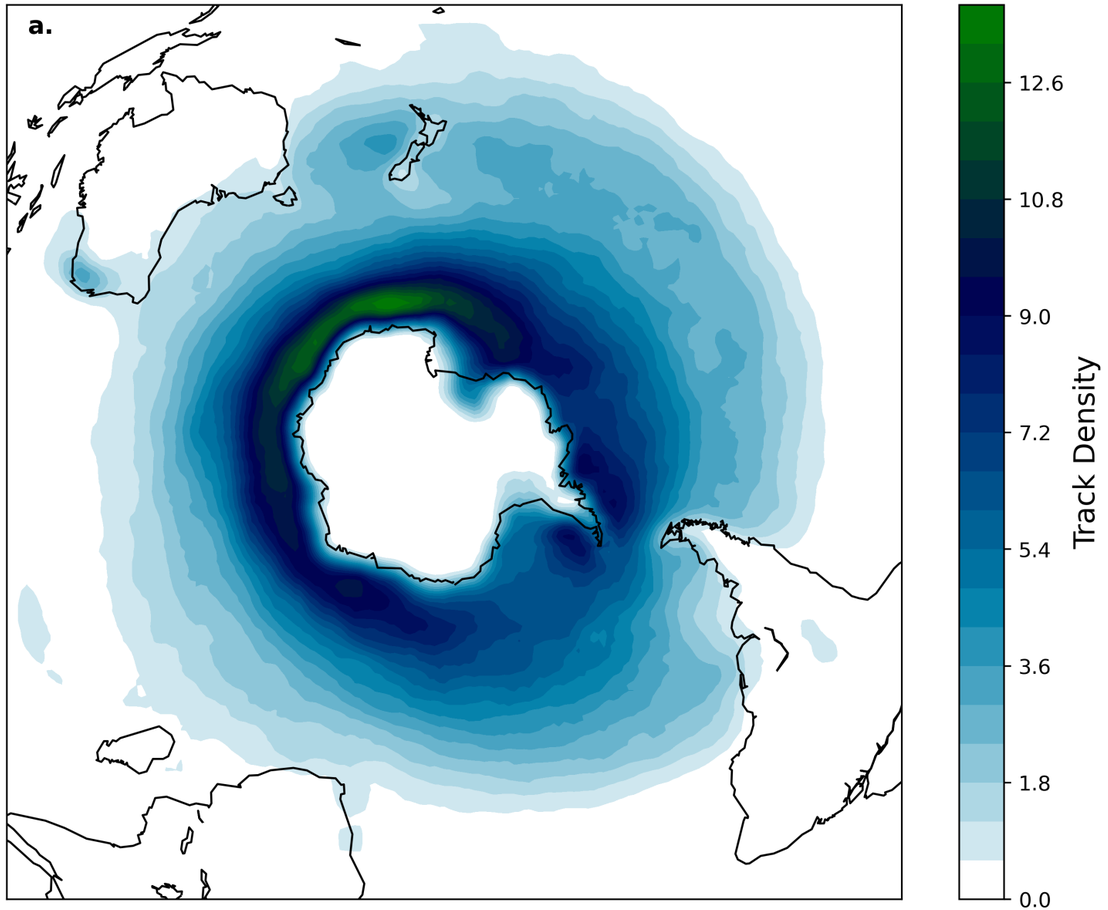
a.

12.6
10.8
9.0
7.2
5.4
3.6
1.8
0.0
Track Density

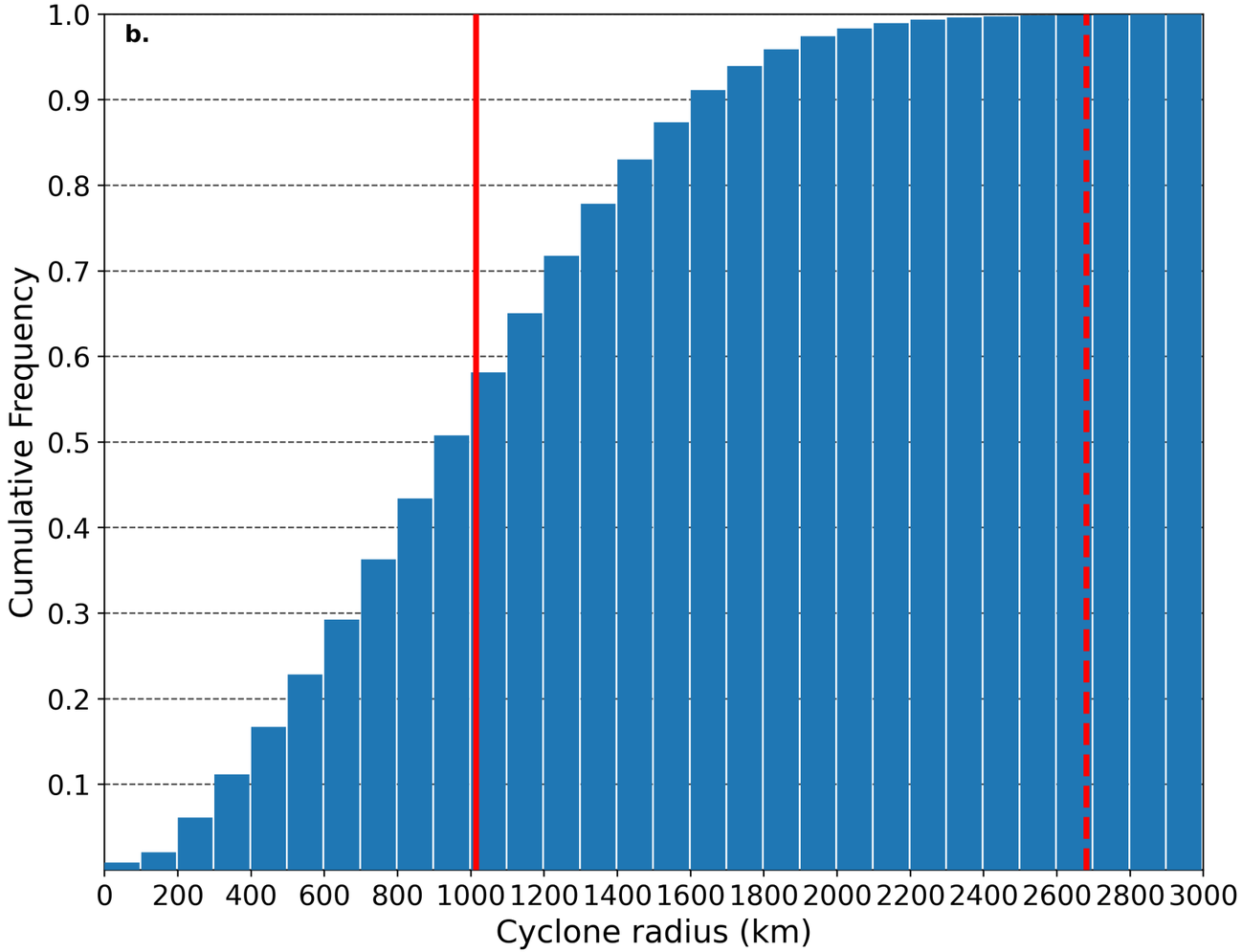
b.
Cumulative Frequency
1.0
0.9
0.8
0.7
0.6
0.5
0.4
0.3
0.2
0.1
0
200
400
600
800
1000
1200
1400
1600
1800
2000
2200
2400
2600
2800
3000
Cyclone radius (km)

Figure 2.

a. ERA5 UV10

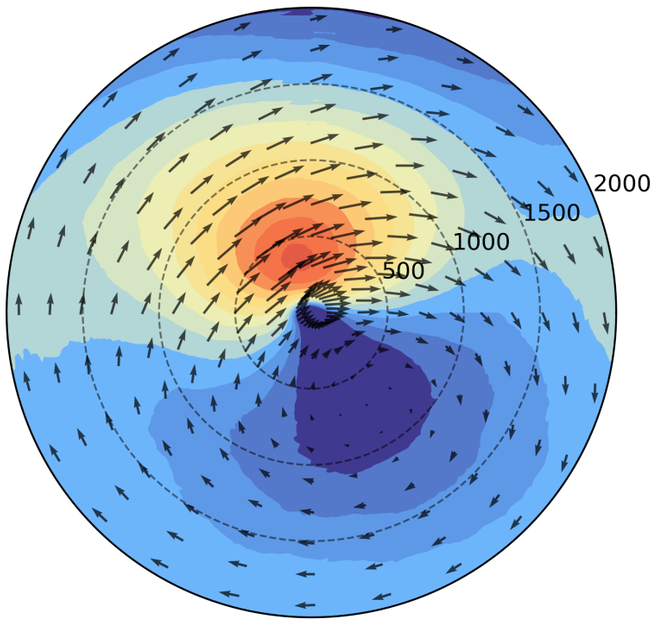

b. WindSat UV10

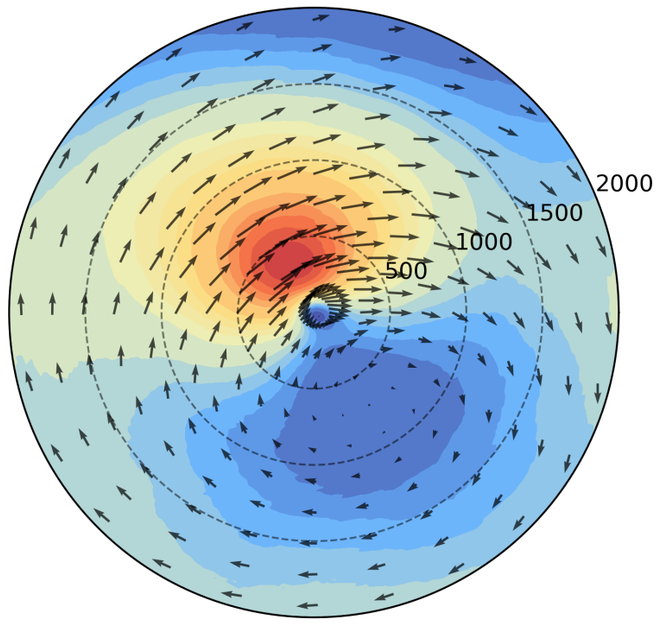

c. Difference

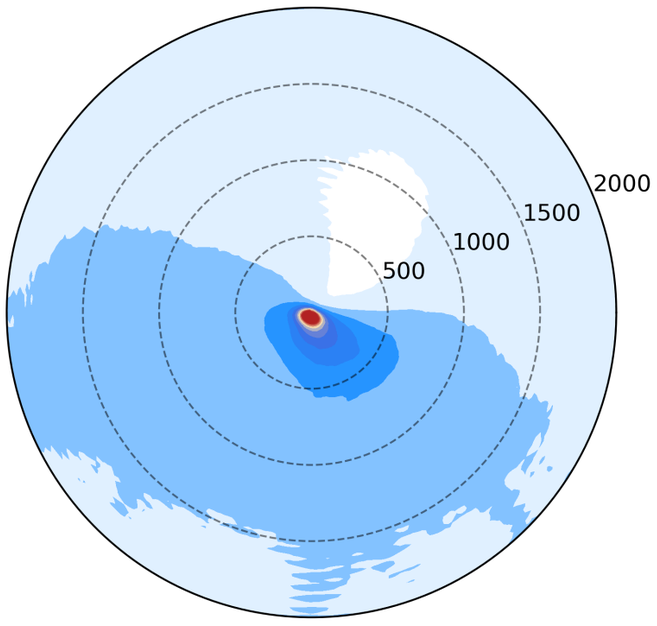

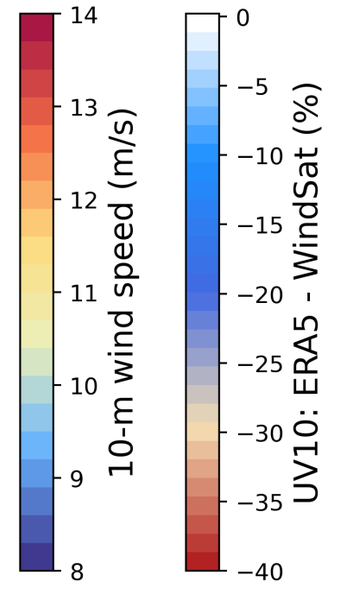

d. ERA5 TCWV

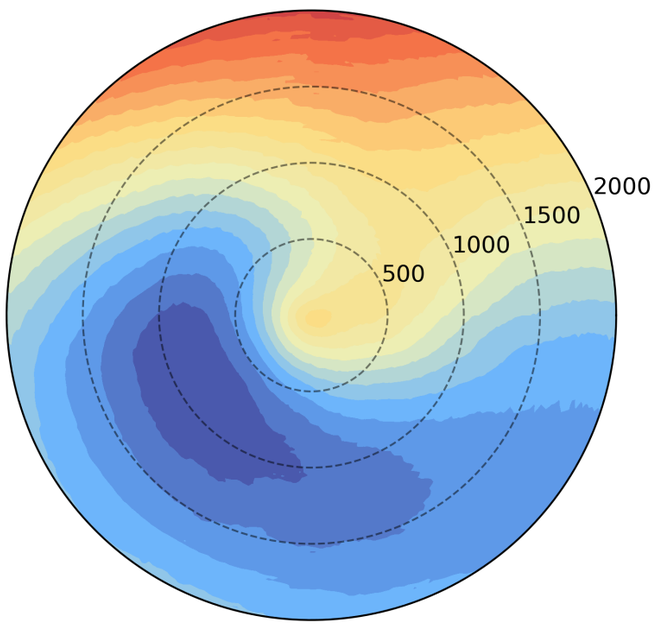

e. WindSat TCWV

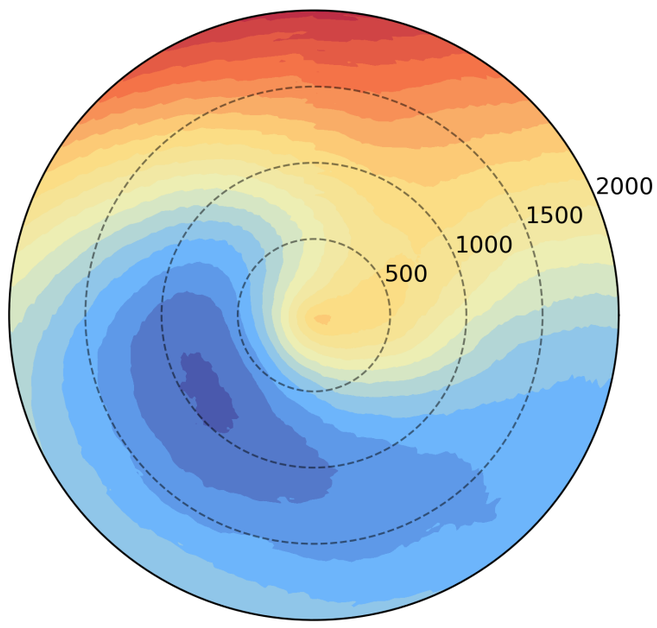

f. Difference

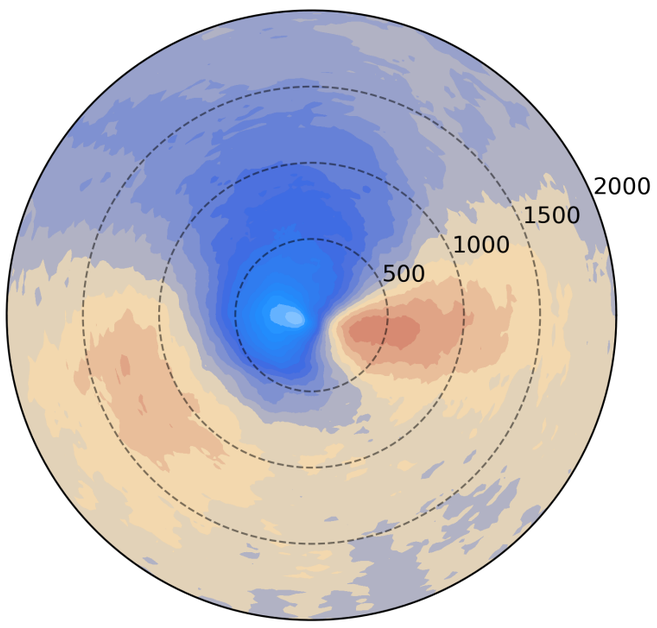

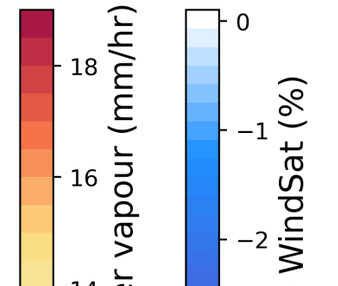

g. ERA5 CLW

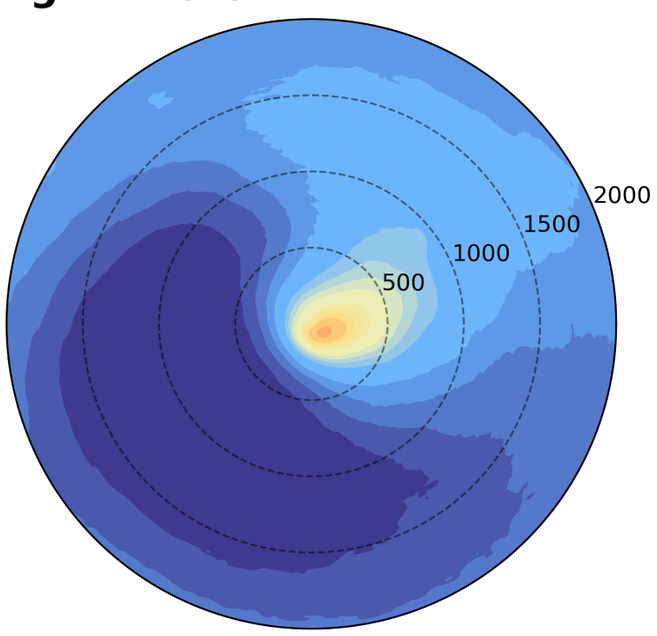

h. WindSat CLW

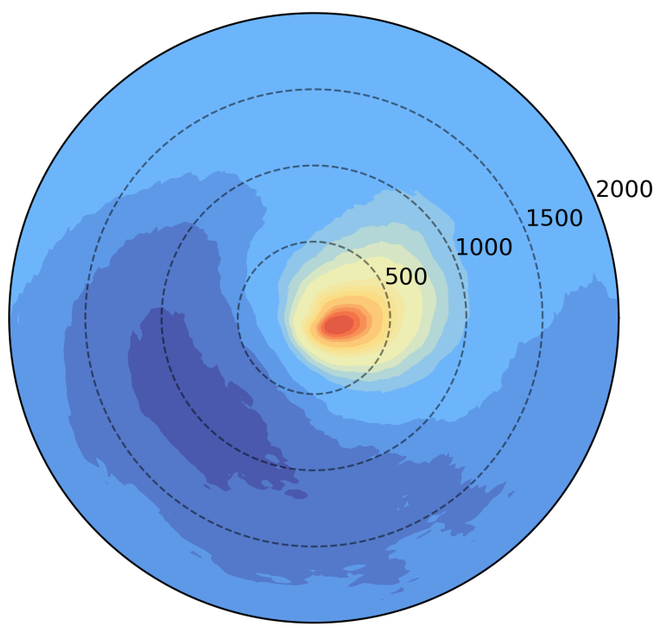

i. Difference

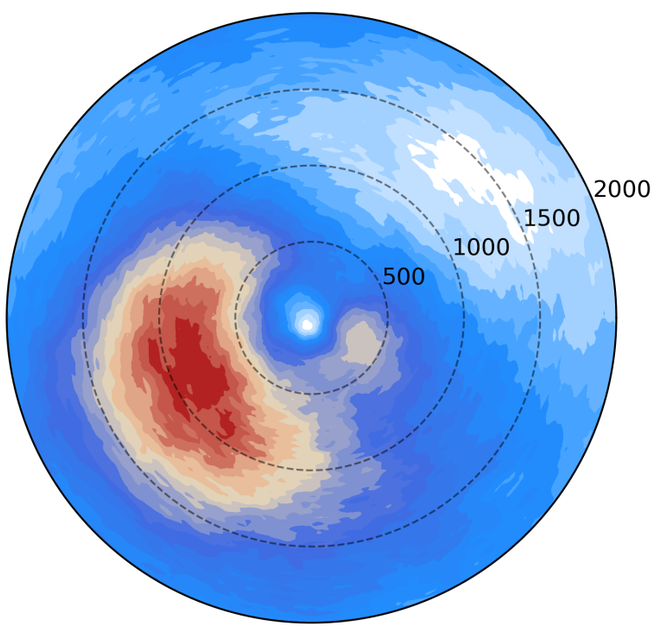

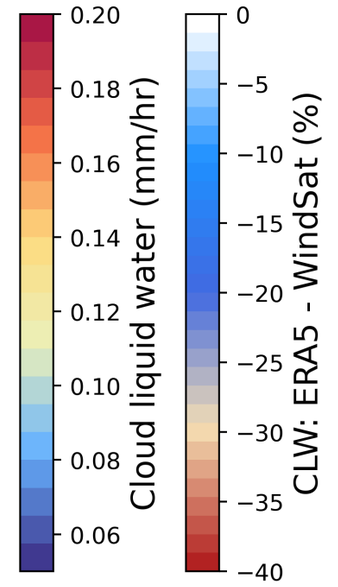

j. ERA5 MTPR

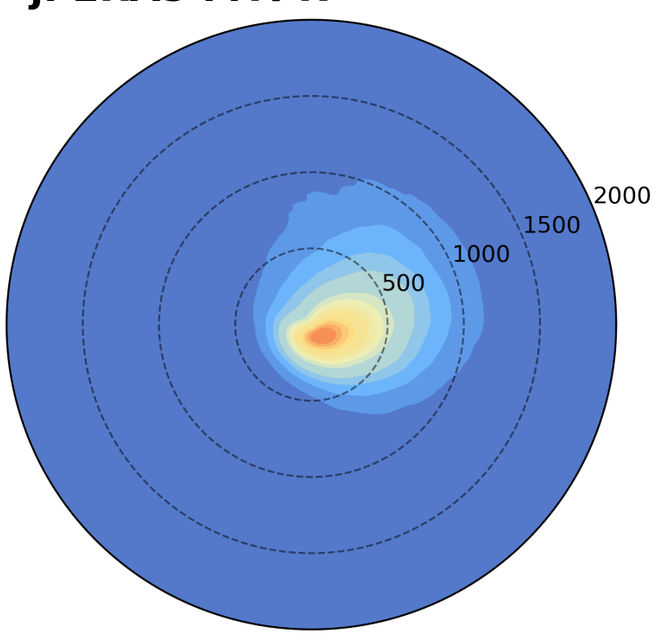

k. WindSat MTPR

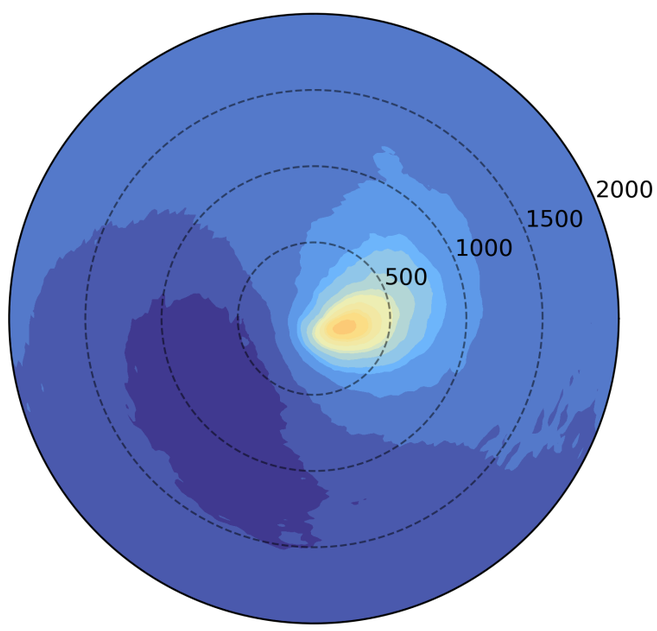

l. Difference

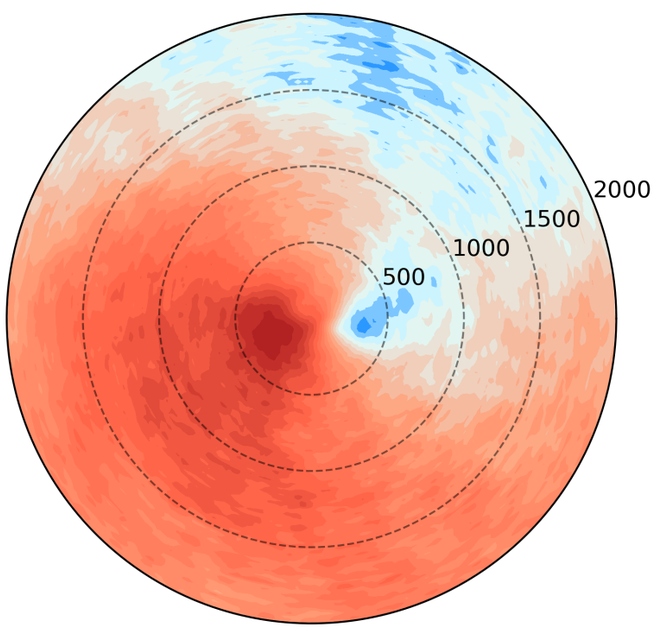

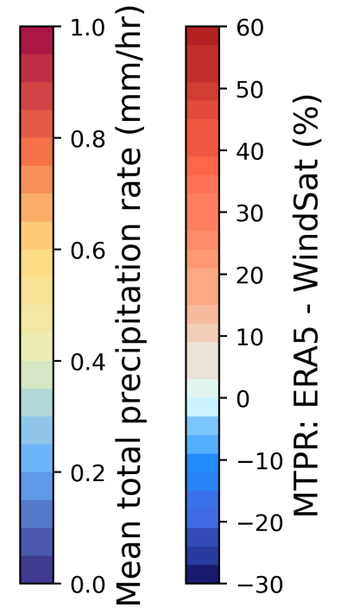

Figure 3.

a. ERA5 TCWV

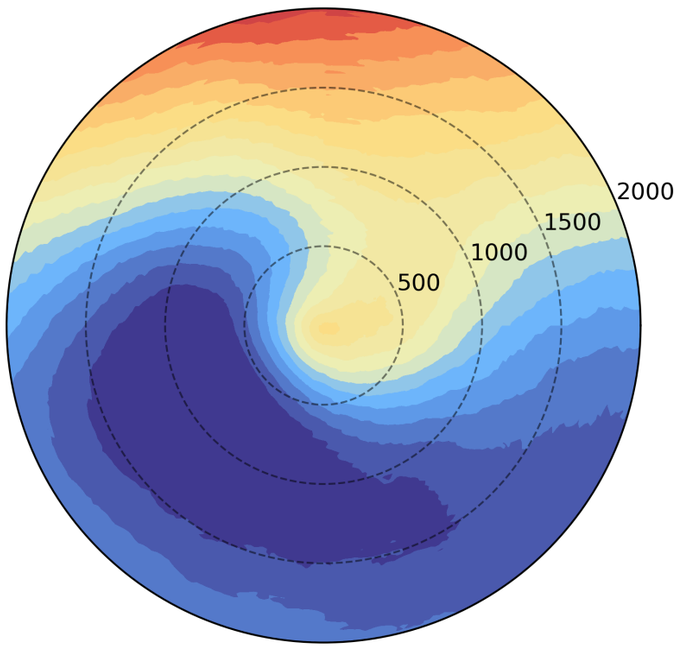

b. AMSR TCWV

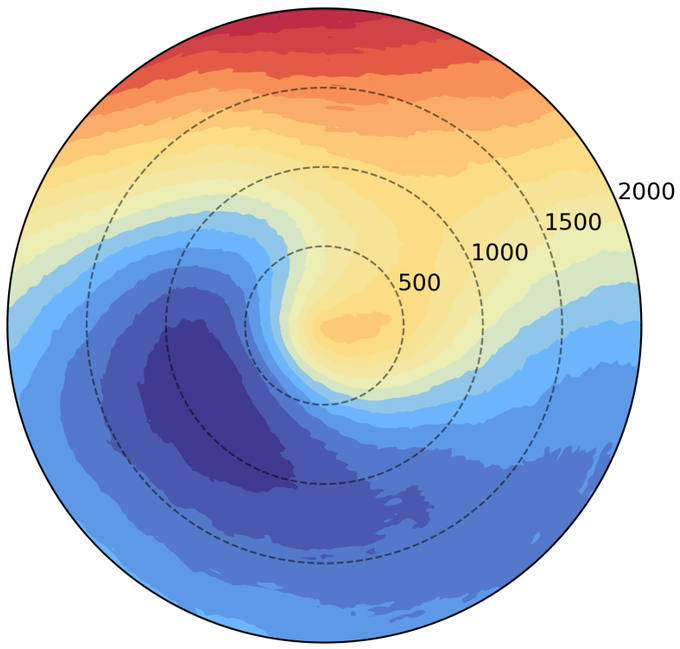

c. Difference

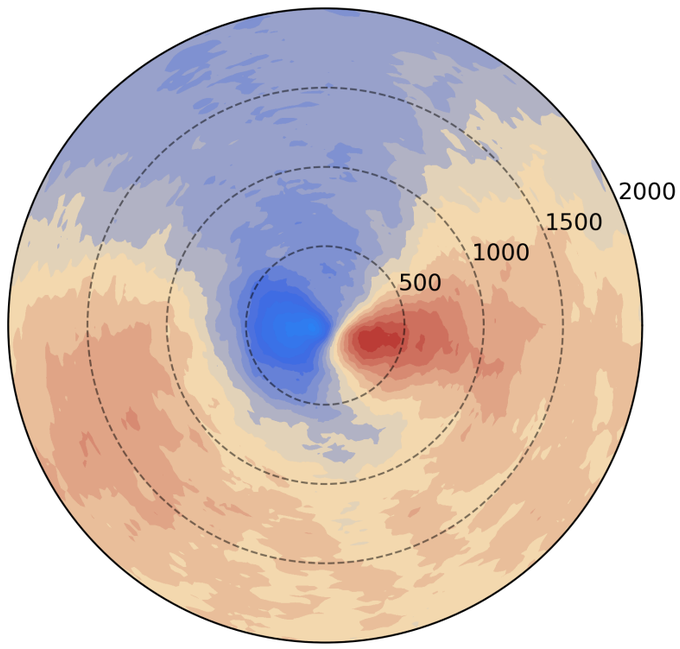

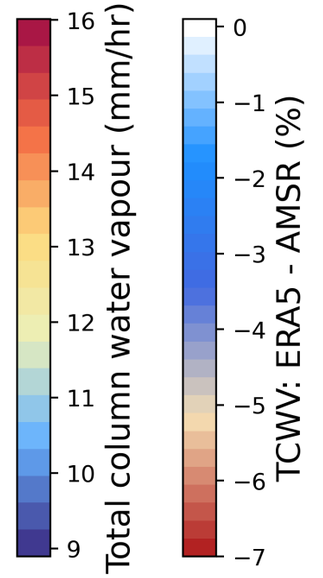

d. ERA5 CLW

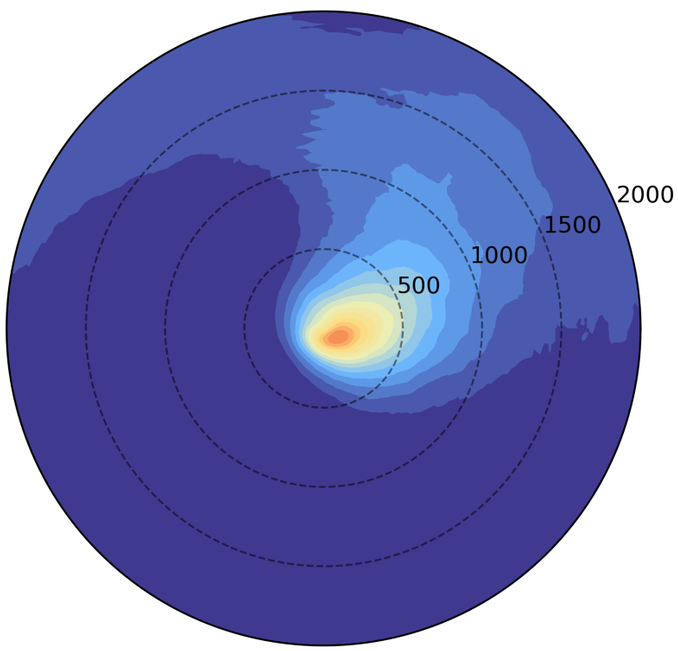

e. AMSR CLW

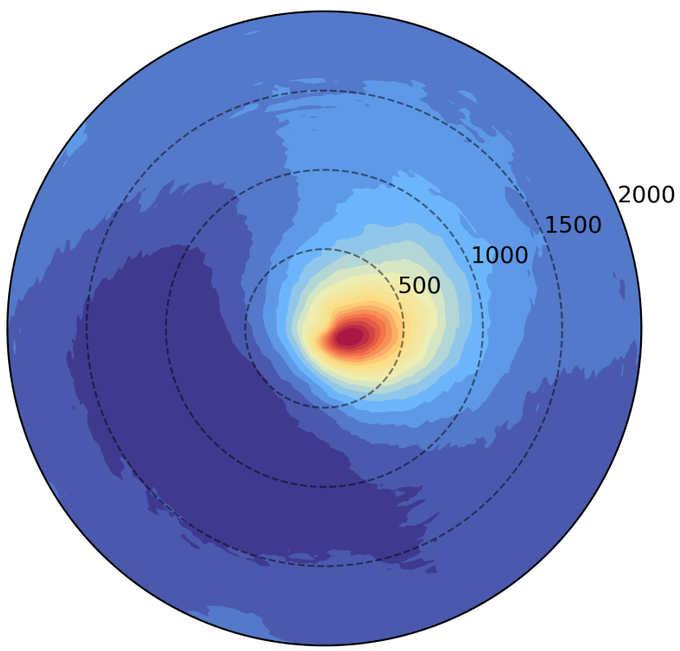

f. Difference

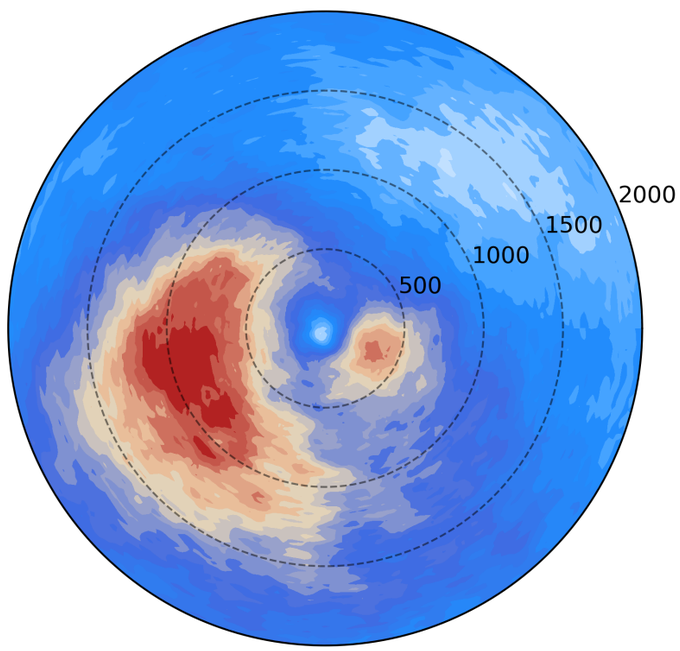

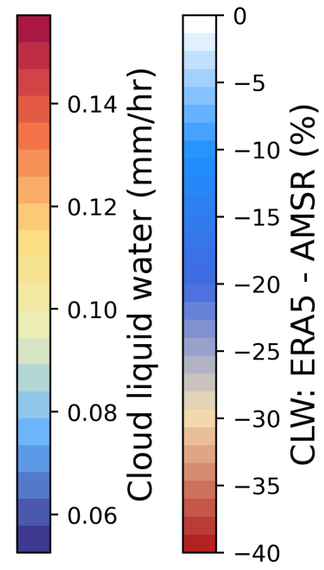

g. ERA5 MTPR

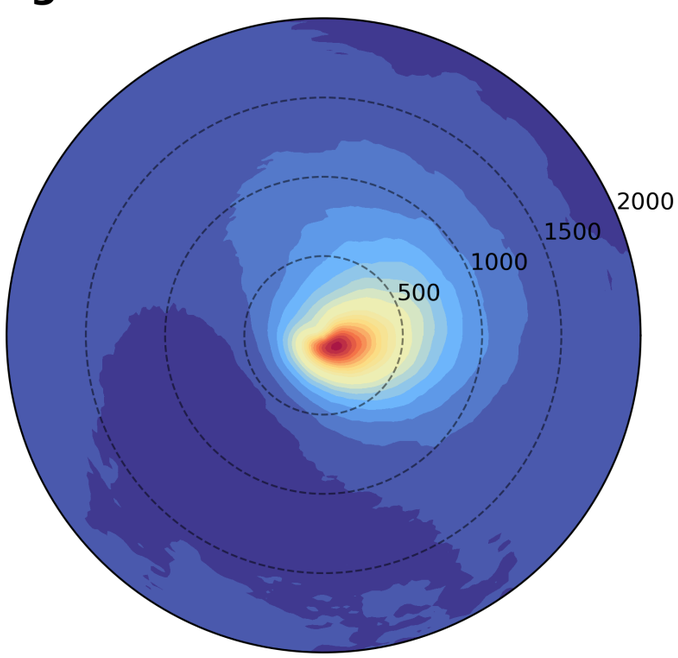

h. AMSR MTPR

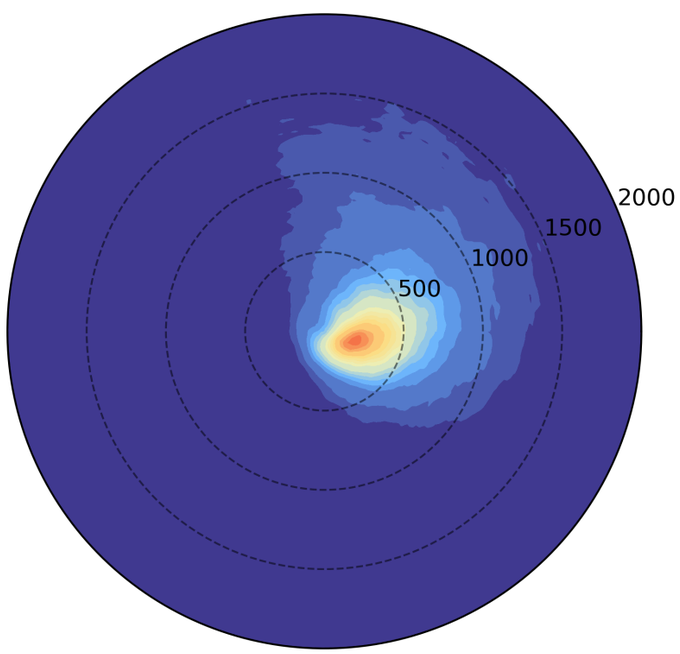

i. Difference

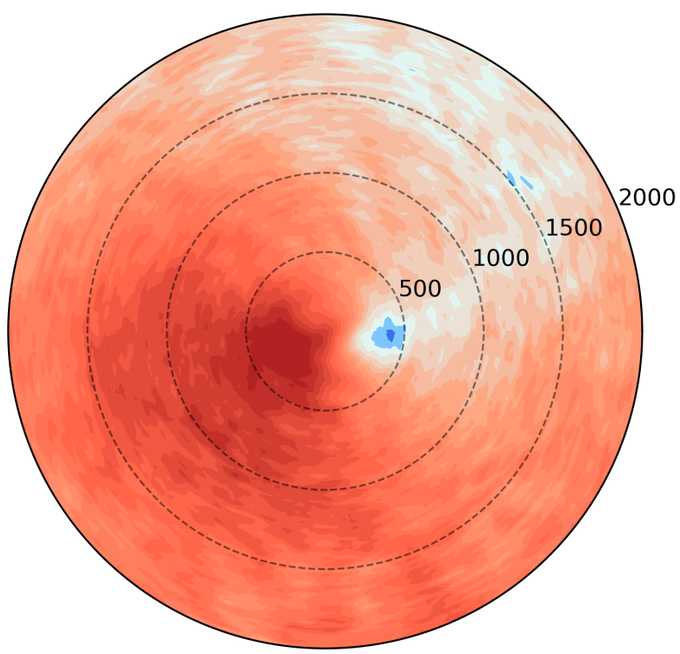

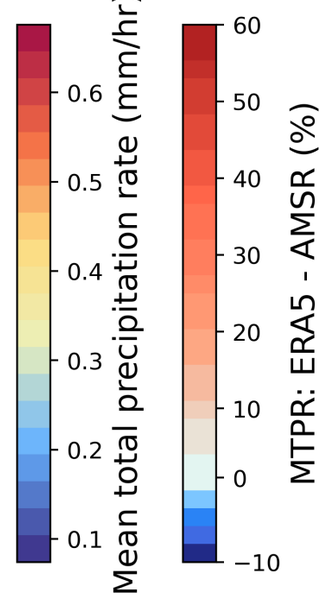

Figure 4.

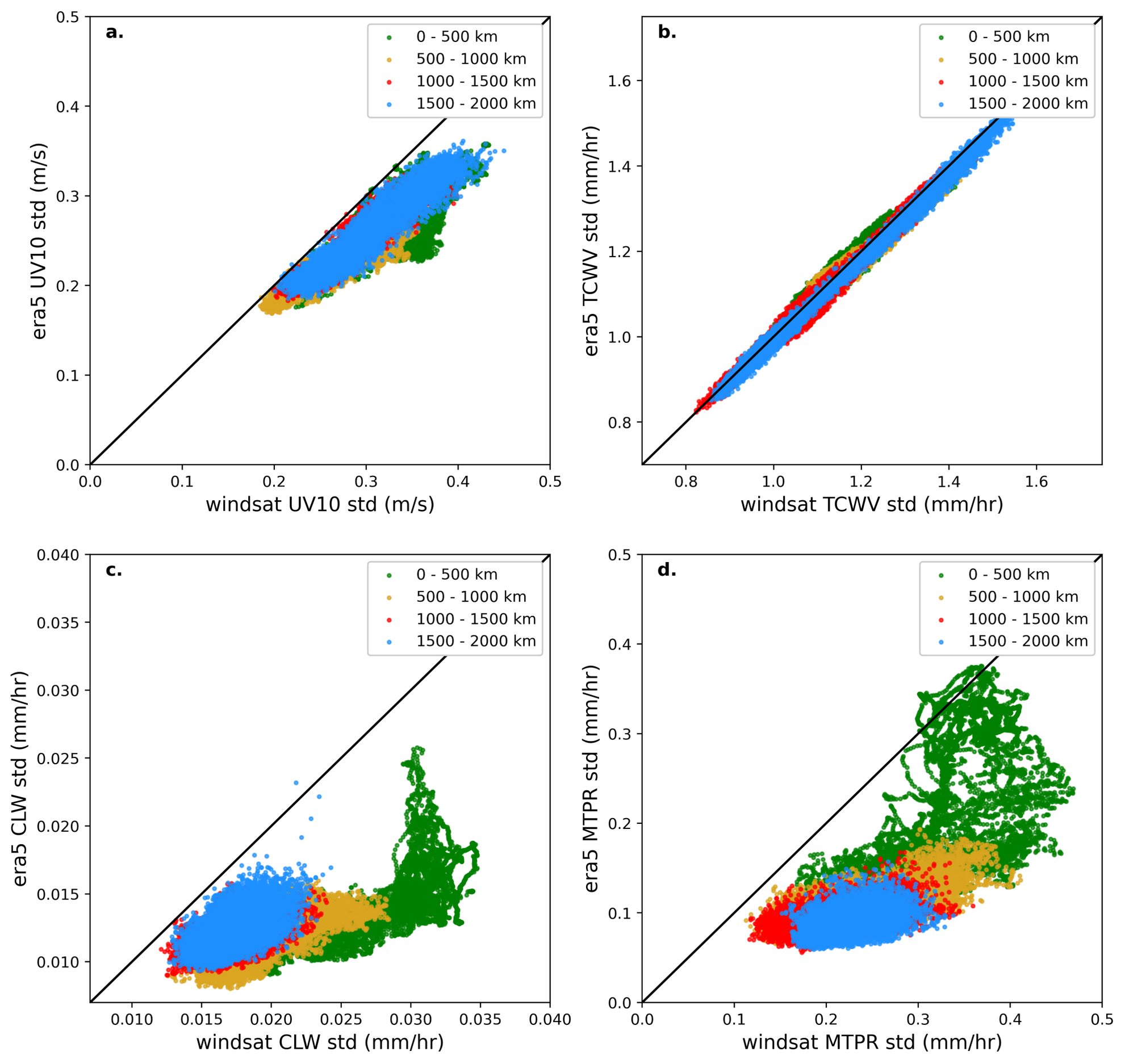
a.
0 - 500 km
500 - 1000 km
1000 - 1500 km
1500 - 2000 km
era5 UV10 std (m/s)
windsat UV10 std (m/s)
0.0
0.1
0.2
0.3
0.4
0.5
b.
0 - 500 km
500 - 1000 km
1000 - 1500 km
1500 - 2000 km
era5 TCWV std (mm/hr)
windsat TCWV std (mm/hr)
0.8
1.0
1.2
1.4
1.6
c.
0 - 500 km
500 - 1000 km
1000 - 1500 km
1500 - 2000 km
era5 CLW std (mm/hr)
windsat CLW std (mm/hr)
0.010
0.015
0.020
0.025
0.030
0.035
0.040
d.
0 - 500 km
500 - 1000 km
1000 - 1500 km
1500 - 2000 km
era5 MTPR std (mm/hr)
windsat MTPR std (mm/hr)

Figure 5.

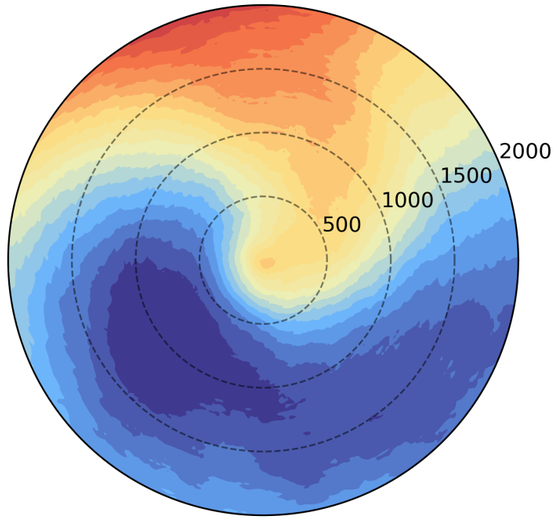

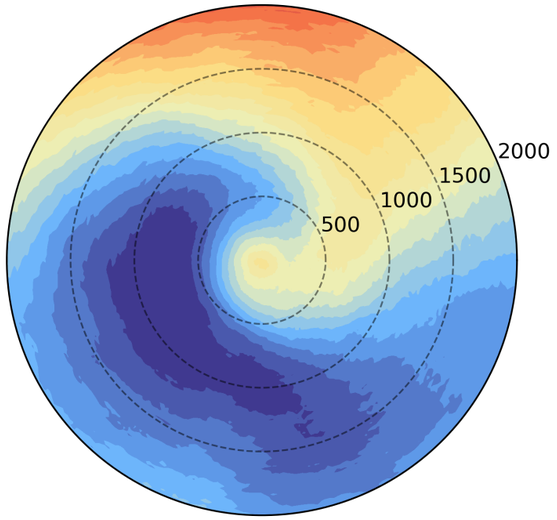

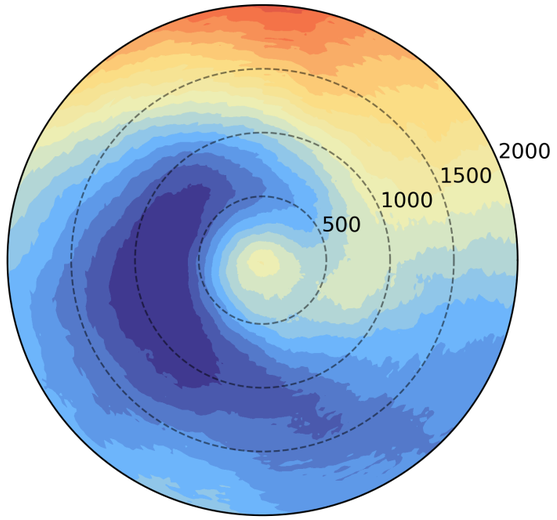

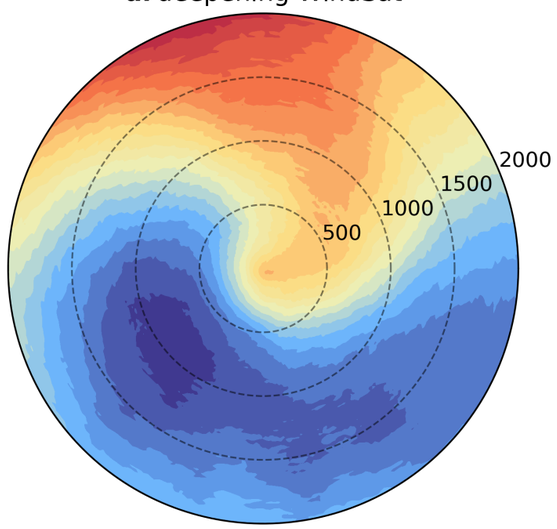

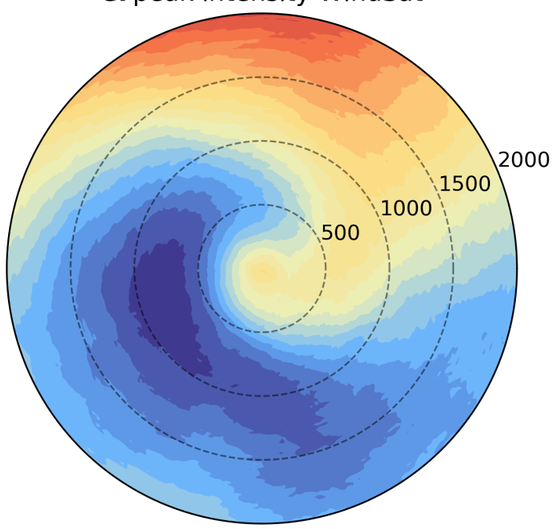

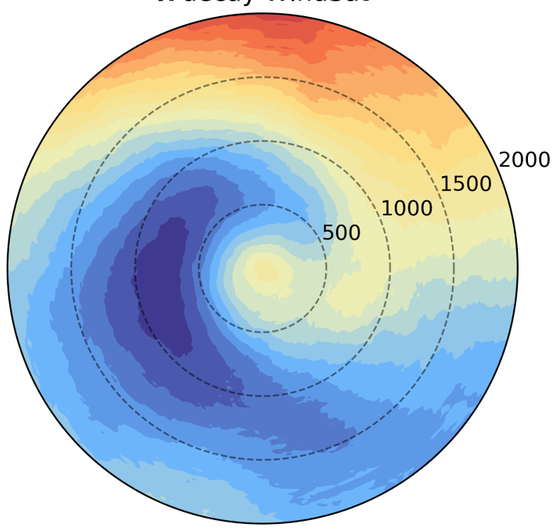

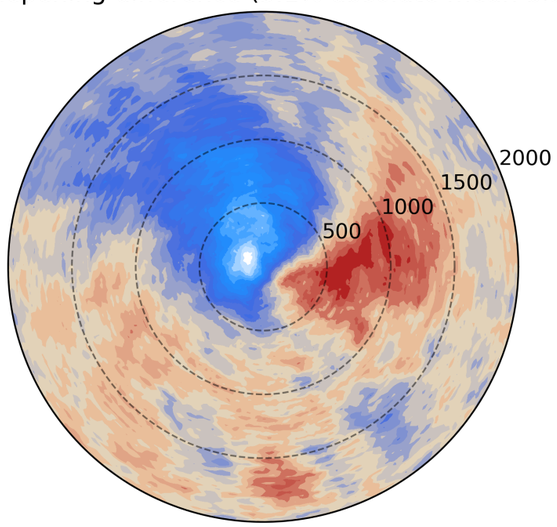

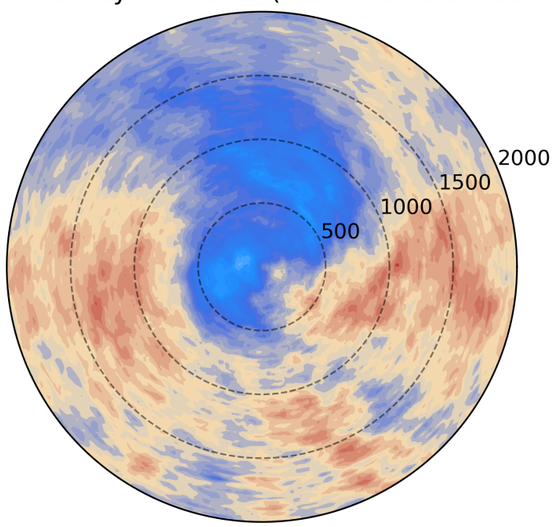

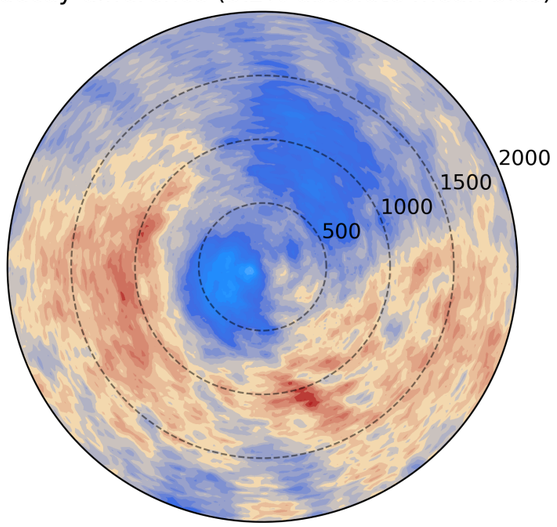

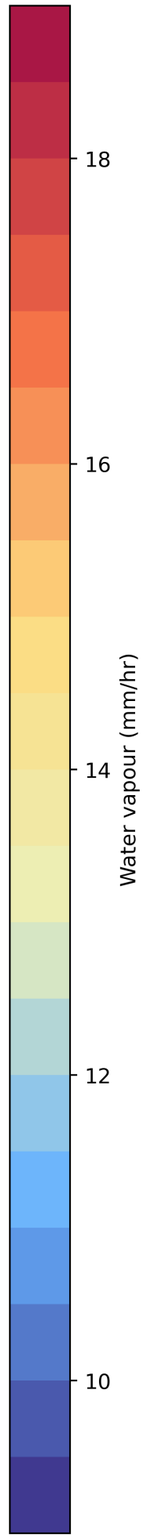

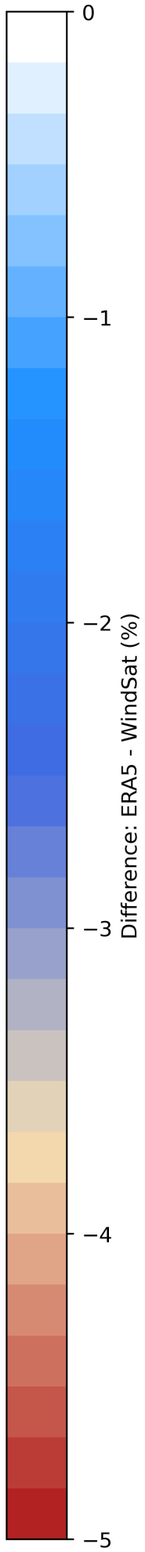

a. deepening ERA5
b. peak intensity ERA5
c. decay ERA5
d. deepening WindSat
e. peak intensity WindSat
f. decay WindSat
g. deepening difference (3.1% absolute mean bias)
h. peak intensity difference (3.1% absolute mean bias)
i. decay difference (3.2% absolute mean bias)
500
1000
1500
2000
Water vapour (mm/hr)
10
12
14
16
18
Difference: ERA5 - WindSat (%)
0
−1
−2
−3
−4
−5

Figure 6.

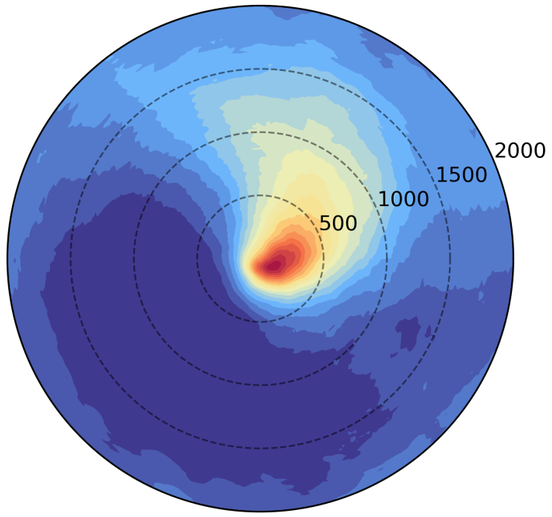

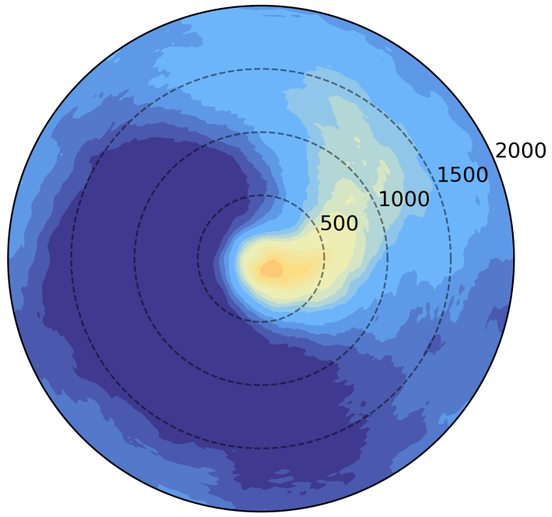

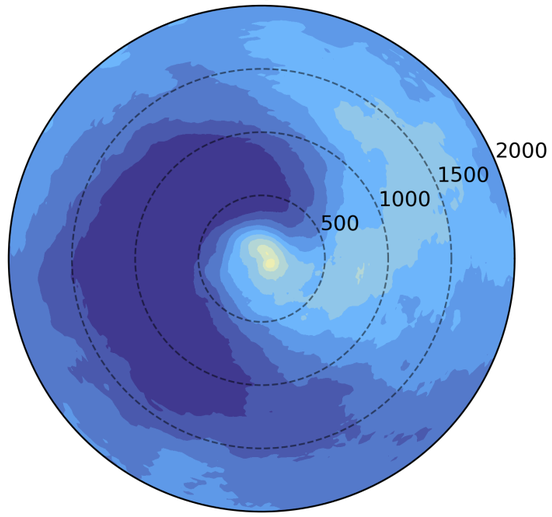

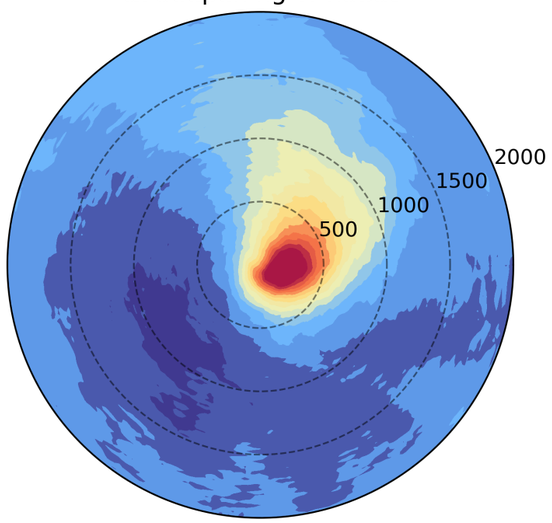

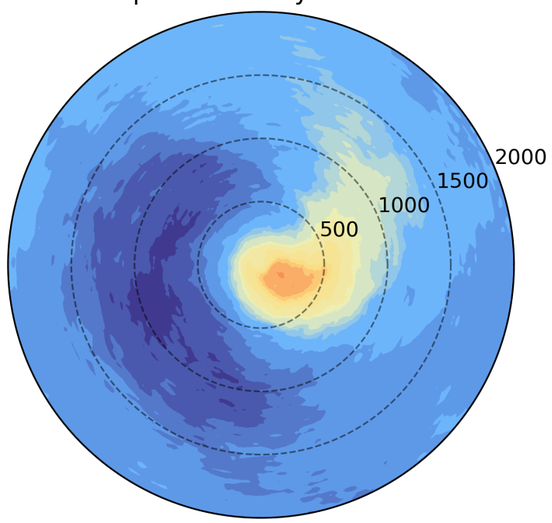

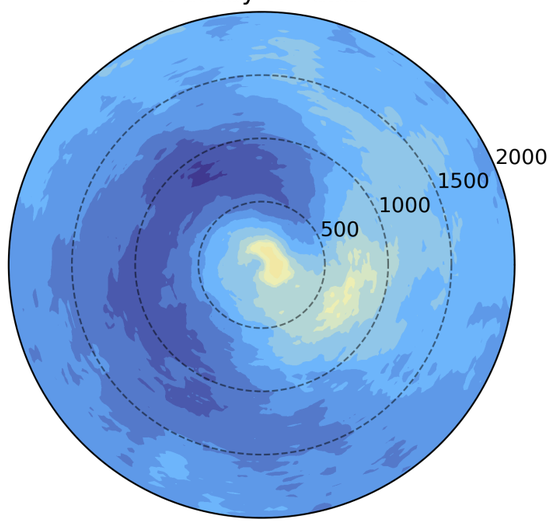

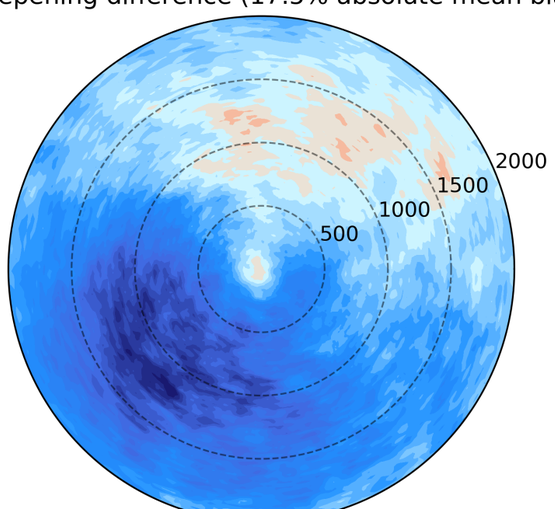

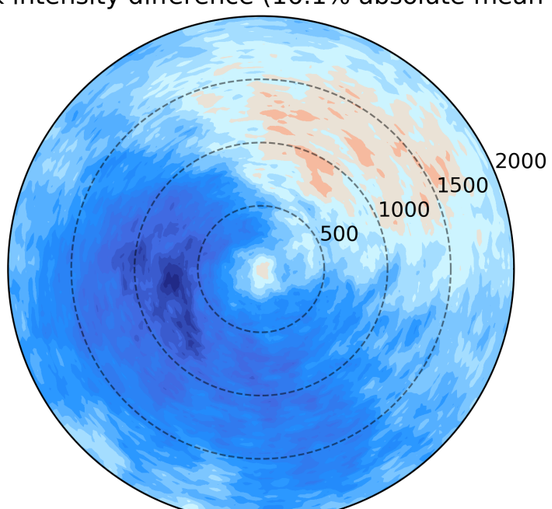

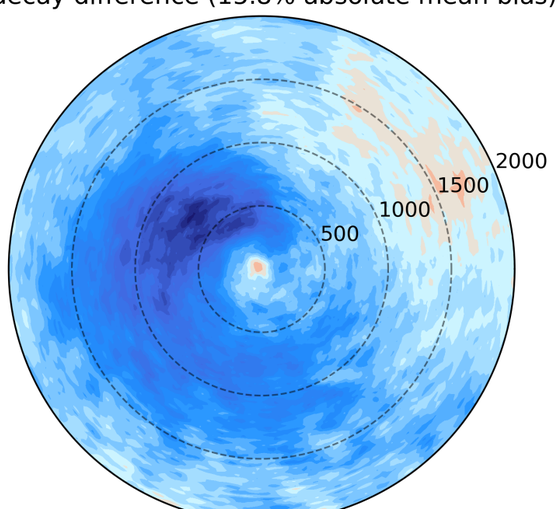

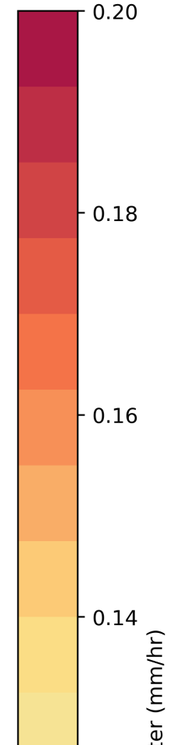

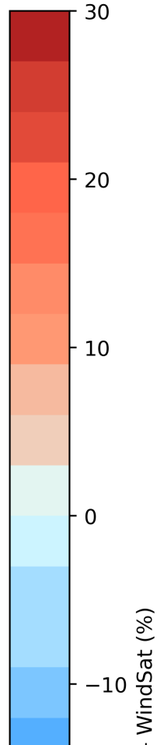

a. deepening ERA5
b. peak intensity ERA5
c. decay ERA5
d. deepening WindSat
e. peak intensity WindSat
f. decay WindSat
g. deepening difference (17.5% absolute mean bias)
h. peak intensity difference (16.1% absolute mean bias)
i. decay difference (15.8% absolute mean bias)
500
1000
1500
2000
Cloud liquid water (mm/hr)
0.06
0.08
0.10
0.12
0.14
0.16
0.18
0.20
Difference: ERA5 - WindSat (%)
−60
−50
−40
−30
−20
−10
0
10
20
30

Figure 7.

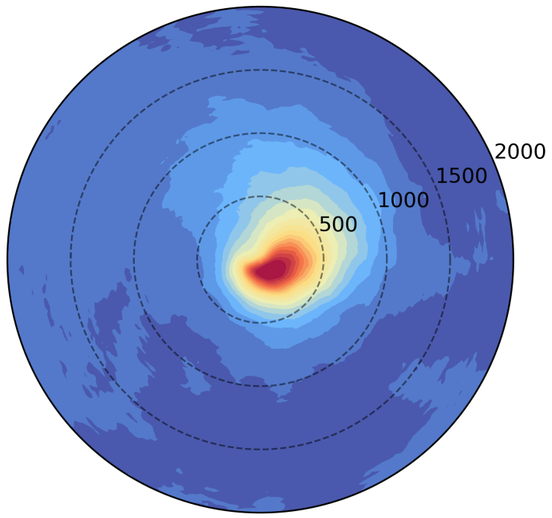

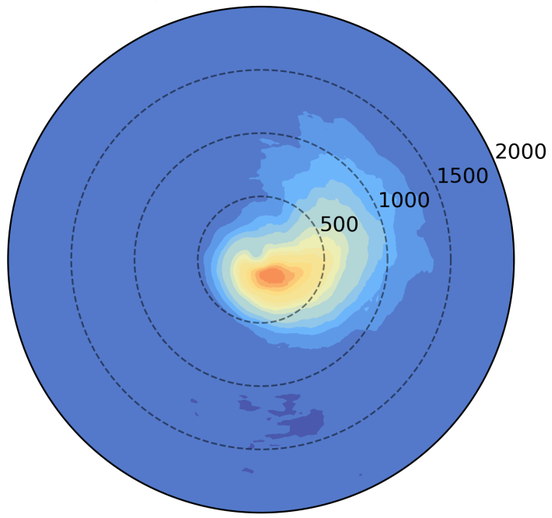

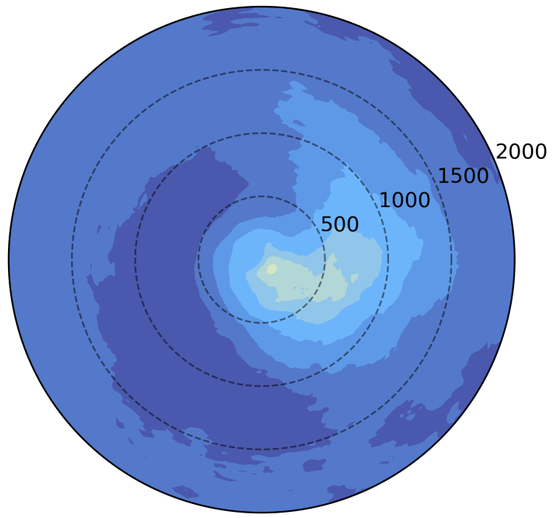

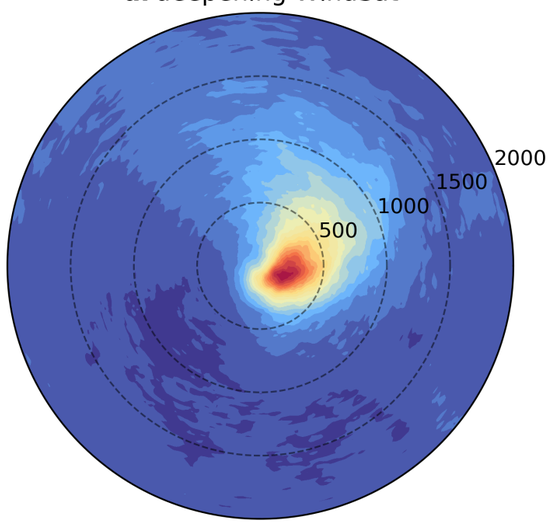

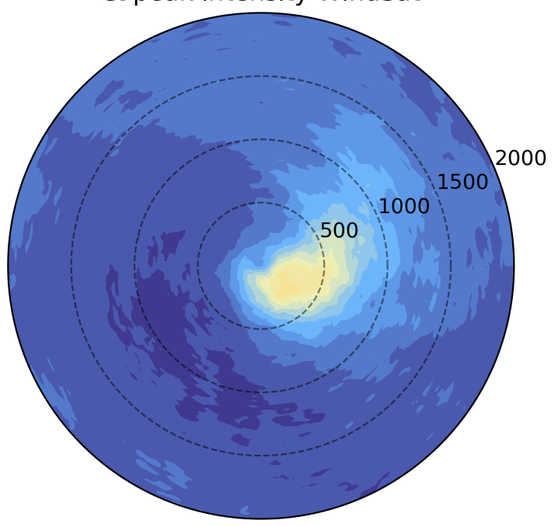

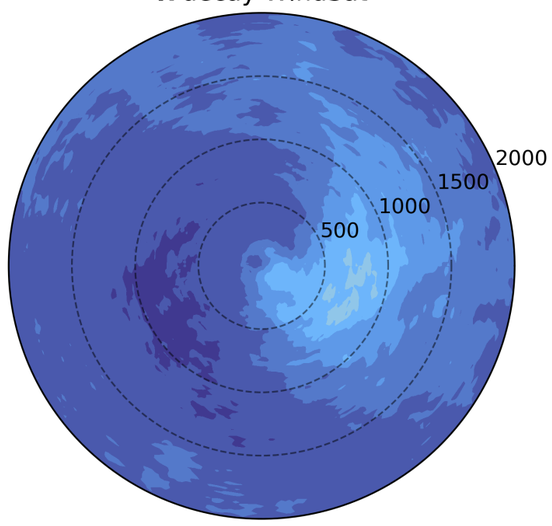

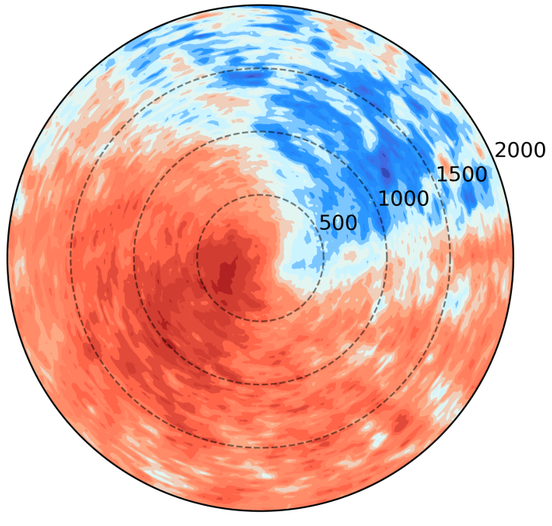

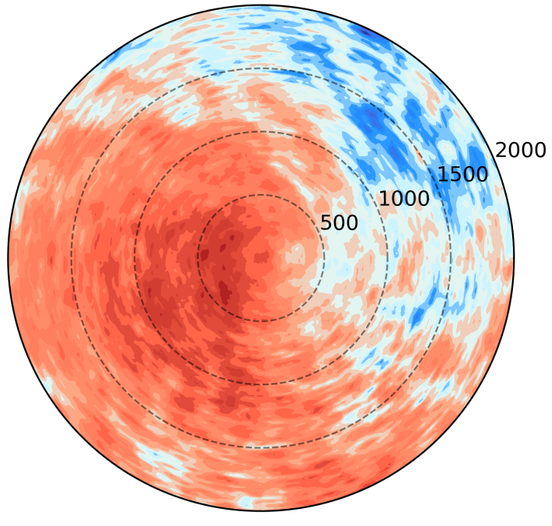

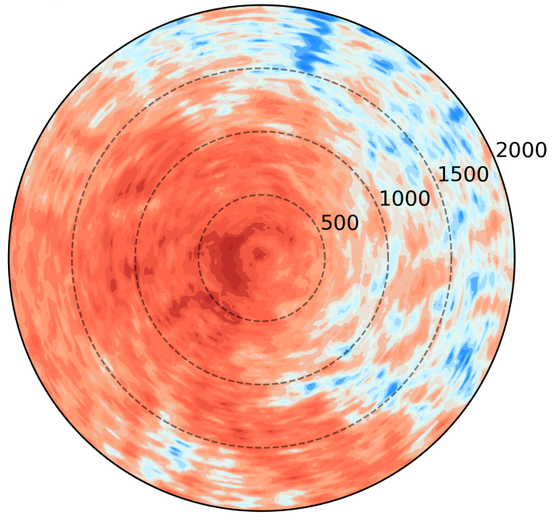

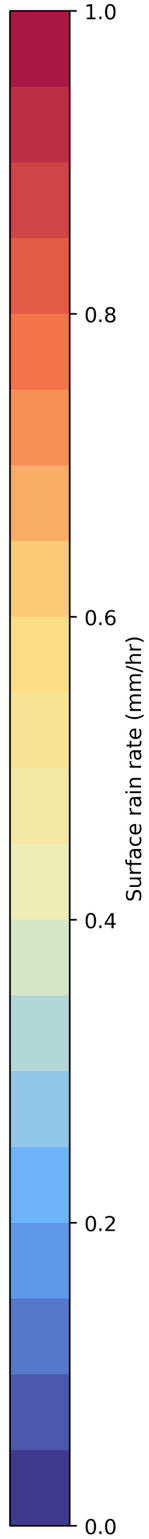

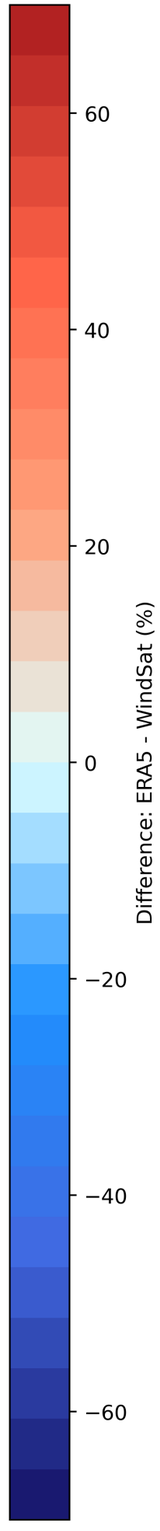

a. deepening ERA5

b. peak intensity ERA5

c. decay ERA5

d. deepening WindSat

e. peak intensity WindSat

f. decay WindSat

g. deepening difference (28.4% absolute mean bias)

h. peak intensity difference (28.7% absolute mean bias)

i. decay difference (29.6% absolute mean bias)

Figure 8.

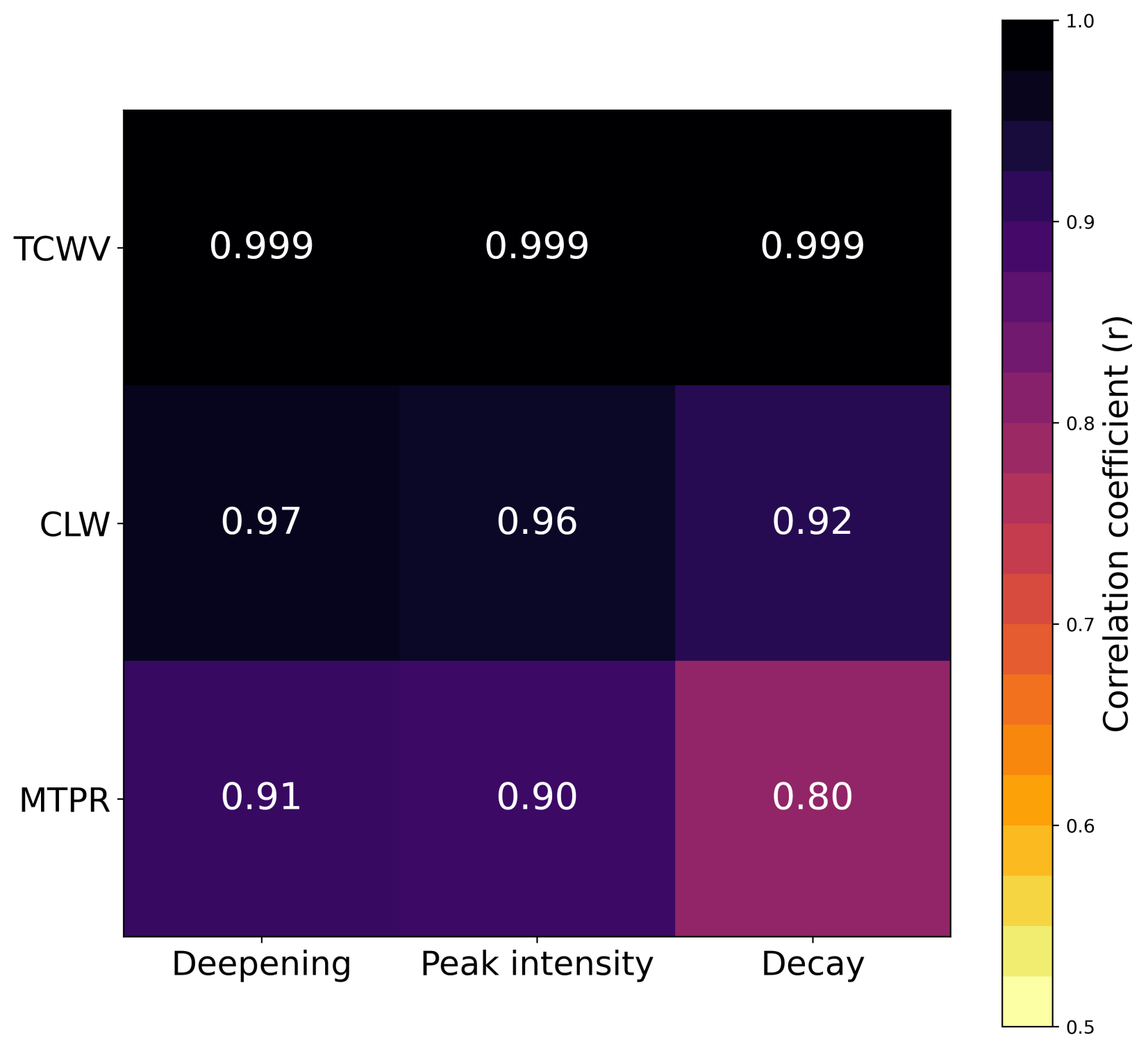
TCWV
CLW
MTPR
0.999
0.999
0.999
0.97
0.96
0.92
0.91
0.90
0.80
Deepening
Peak intensity
Decay
Correlation coefficient (r)
1.0
0.9
0.8
0.7
0.6
0.5